Journal of Materials Chemistry A

REVIEW

View Article Online
View Journal | View Issue

Cite this: J. Mater. Chem. A, 2017, 5, 1873

Energy conversion technologies towards self-powered electrochemical energy storage systems: the state of the art and perspectives

Huige Wei,*[a] Dapeng Cui,*[b] Junhui Ma,[a] Liqiang Chu,[a] Xiaoyu Zhao,[a] Haixiang Song,[c] Hu Liu,[c] Tao Liu,[d] Ning Wang*[d] and Zhanhu Guo*[c]

Received 10th November 2016
Accepted 5th December 2016

DOI: 10.1039/c6ta09726j

www.rsc.org/MaterialsA

Energy conversion and storage are considered two of the most important technologies in today's green and sustainable energy science. Conjugating energy harvest and storage to fabricate self-powered electrochemical energy storage systems (SEESs) that harvest their operating energy from the environment holds great promise to power future portable and wearable electronics. SEESs represent a new trend in energy technologies. This review paper provides an overview of recent advances in SEESs powered by different energy conversion technologies with an emphasis on state-of-art organic solar cells, nanogenerators, and hybrid cells. Future challenges and perspectives of SEESs are also discussed.

1. Introduction

Global warming and the depletion of fossil fuels have imposed serious threats to the sustainable development of humankind.[1,2] To address these challenges, extensive research efforts have been devoted to the exploration and utilization of energy from solar, wind, tidal, geo-thermal and other alternative and renewable energy sources.[3–5] Given the intermittent nature of these energy resources, reliable energy storage systems are necessary to store and deliver the harvested electricity in a stable and controlled manner.[6] Among the numerous energy storage systems such as pumped hydro storage, compressed air energy storage, and flywheel energy storage, electrochemical energy storage (EES) systems are a key and dominating member that has attracted increasing attention.[7–10]

Rechargeable batteries and supercapacitors (SCs, or electrochemical capacitors) are two important technological subclasses of EES system which have found a broad range of applications. Currently, lithium-ion batteries (LIBs) are reigning

[a]College of Chemical Engineering and Materials Science, Tianjin University of Science and Technology, Tianjin 300457, China. E-mail: huigewei@tust.edu.cn

[b]College of Packing and Printing Engineering, Tianjin University of Science and Technology, Tianjin, 300222 China. E-mail: dapeng@tust.edu.cn

[c]Integrated Composites Laboratory (ICL), Department of Chemical and Biomolecular Engineering, University of Tennessee, Knoxville, TN 37996, USA. E-mail: nanomaterials2000@gmail.com; zguo10@utk.edu

[d]State Key Laboratory of Marine Resource Utilization in South China Sea, Hainan University, Haikou, Hainan 570228, China. E-mail: wangninguestc@gmail.com

Dr Huige Wei, currently an Assistant Professor in the College of Chemical Engineering and Materials Science at Tianjin University of Science and Technology, Tianjin, China, obtained her PhD degree from Dan F. Smith at the Department of Chemical Engineering, Lamar University, USA (2015). Her current research focuses on multifunctional composites for energy conversion and storage applications.

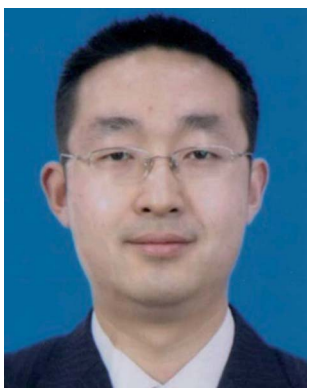

Dr Dapeng Cui, currently an Assistant Professor in the College of Packing and Printing Engineering at Tianjin University of Science and Technology, Tianjin, China, obtained his PhD degree from the Department of Chemistry and State Key Laboratory of Applied Organic Chemistry, Lanzhou University, China. He received three-years' (2011–2014) postdoctoral training in the Laboratory of New Materials, Institute of Chemistry, Chinese Academy of Sciences, Beijing, China. His current research focuses on conductive ink and printable solar cells & supercapacitors.

over the rechargeable battery markets even though other types of rechargeable batteries such as sodium-ion batteries,[11,12] magnesium-ion batteries,[13,14] and aluminum-ion batteries[15,16] are emerging. Both LIBs and SCs rely on electrochemical processes but follow different working principles, and therefore exhibit distinct charge-storage properties.[17] LIBs are based on diffusion-controlled faradic reactions occurring in the bulk electrodes, and thus can be slow (Fig. 1A).[18] The bulk energy storage mechanism provides LIBs with high energy densities (as high as 180 W h kg^{-1} (ref. 19)) but at the same time LIBs have limited power densities; their lifetime is also very short, usually several hundred cycles. Differing from LIBs, SCs store the electrical energy *via* either fast reversible adsorption at the electrode/electrolyte interface (electrochemical double layer capacitors, EDLCs, see Fig. 1B),[19] or quick redox reactions at/near the surface (pseudocapacitors, see Fig. 1C).[20–24] Therefore, SCs offer great advantages of higher power density (>10 kW kg^{-1} (ref. 25)), exceptionally long cycling life (>10^5 cycles) and much greater reliability. Unfortunately, their energy densities are much lower compared to those of LIBs, usually less than 10 W h kg^{-1} for commercialized SCs.[26] Research efforts have been directed toward improving the performances of current LIBs and SCs[17,27] or developing new EES technologies, for example, lithium-ion hybrid supercapacitors (LIHSs)[28–30] to meet the increasingly stringent requirements of future portable electronics.

Meanwhile, the development of sustainable self-powered or self-sufficient systems that harvest their operating energy from the environment holds great promise to power future portable and wearable electronics.[33–35] In particular, self-powered

Dr Li-Qiang Chu received his BSc from Lanzhou University, China (1997) and then worked as a research assistant at the Dalian Institute of Chemical Physics. He obtained his MSc from the National University of Singapore, Singapore (2004) and PhD from the Max-Planck-Institute for Polymer Research, Germany (2007). He then worked as a postdoctoral fellow at the University of Notre Dame (2008–2010) and the University of California, Davis (2010–2011). He then started as a full professor of materials science at Tianjin University of Science & Technology, China (2011). His research interests include polymeric biomaterials, surface plasmon optics, PECVD and portable biosensors.

Dr Xiaoyu Zhao, currently an Assistant Professor in the College of Chemical Engineering and Materials Science at Tianjin University of Science and Technology, Tianjin, China, obtained his PhD degree from the University of Fukui, Japan (2014). His current research focuses on the fundamentals and applications of electrochemistry.

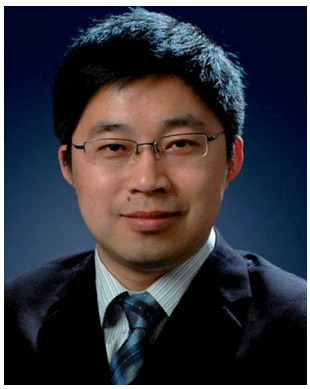

Dr Ning Wang, currently a Full Professor at the State Key Laboratory of Marine Resource Utilization in South China Sea, Hainan University, China, obtained a PhD degree in Materials Science and Engineering from Tsinghua University, China (2007) and received two-years' (2008–2010) postdoctoral training in the Department of Applied Chemistry at Nagoya University, Japan. Dr Wang is currently an executive deputy director of State Key Laboratory of Marine Resource Utilization in South China Sea, Hainan University. His current research focuses on the fundamental science for nanomaterials applied in energy-related materials and devices, such as perovskite solar cells, dye-sensitized solar cells and thermoelectric materials.

Dr Zhanhu Guo, currently an Associate Professor in the Department of Chemical and Biomolecular Engineering, University of Tennessee, Knoxville, USA, obtained a PhD degree in Chemical Engineering from Louisiana State University (2005) and received three-years' (2005–2008) postdoctoral training from the Mechanical and Aerospace Engineering Department at the University of California Los Angeles. Dr Guo chaired the Composite Division of the American Institute of Chemical Engineers (AIChE, 2010–2011) and directs the Integrated Composites Laboratory. His current research focuses on multifunctional nanocomposites for electronic devices; energy storage, conversion and saving units; and environmental remediation applications.

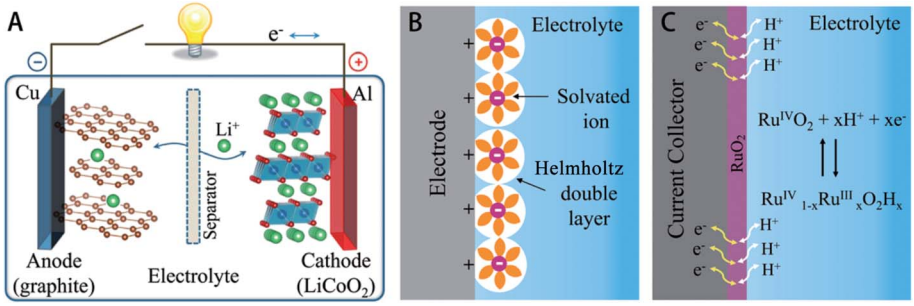

Fig. 1 Working mechanism of (A) a LIB ($LiCoO_2/Li^+$ electrolyte/graphite),[31] (B) an EDLC, and (C) a pseudocapacitor.[32] Reprinted with permission from ref. 31 and 32. Copyright (2013) American Chemical Society.

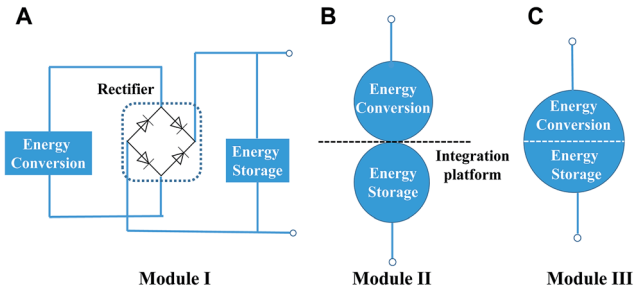

Fig. 2 Three modules of SEESs: the energy conversion and storage units are (A) connected *via* external circuits, (B) connected *via* an integration platform (another electrode), and (C) integrated into one single unit.

electrochemical energy storage systems (SEESs), in which EES components are powered by energy conversion technologies, are becoming highly desirable and represent a new trend in energy technologies.[36–43]

Until now, versatile energy conversion technologies that scavenge energy from individual or multiple sources have been developed to provide a driving force for SEESs.[44,45] Typical examples include solar cells to harvest solar energy,[46] nanogenerators (NGs, a newly emerging field of nano-energy that involves the application of nanomaterials and nanotechnology to harness large- or small-scale mechanical/thermal energy from the surroundings),[47] and hybrid cells (HCs, multi-mode energy harvesters that utilize power from multiple energy sources).[48]

SEESs, defined by the connection module between the energy storage system and the energy conversion system, generally fall into three categories: (1) module I, where the energy conversion and storage units are connected *via* an external circuit, and a capacitor filter, transformer or current converter (*e.g.* a rectifier) may be included in the circuit for optimum output performance (Fig. 2A); (2) module II, *i.e.* the energy conversion and storage units are connected *via* an integration platform (three-electrode module, see Fig. 2B); (3) module III, that is, the energy conversion and storage units are hybridized into one single device (two-electrode module, see Fig. 2C). In the first two modules, the energy conversion and storage processes are independent, *i.e.* the scavenged energy is converted into electricity and then transferred to a SC or LIB for storage, whereas in the third module these two processes are integrated into one step in which the energy is directly converted and simultaneously stored as electrochemical

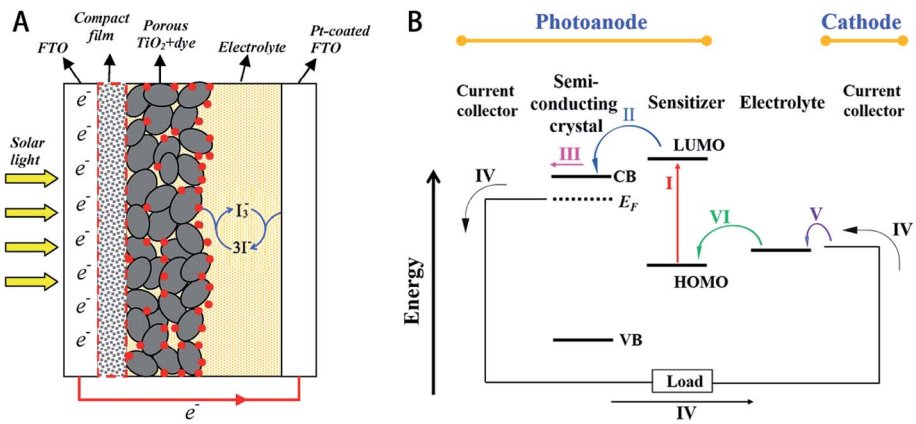

Fig. 3 (A) Schematic structure[65] and (B) energy diagram[66] of a DSC. CB and VB represent the conduction and valence band of the semi-conducting crystal, respectively. E_F below the CB refers to the Fermi level of the semi-conducting crystal at a high degree of electronic doping. LUMO and HOMO are short for the lowest unoccupied and highest occupied molecular orbitals of the sensitizer, respectively. Redrawn from ref. 65. Reprinted from ref. 66 with permission. Copyright (2014) American Chemical Society.

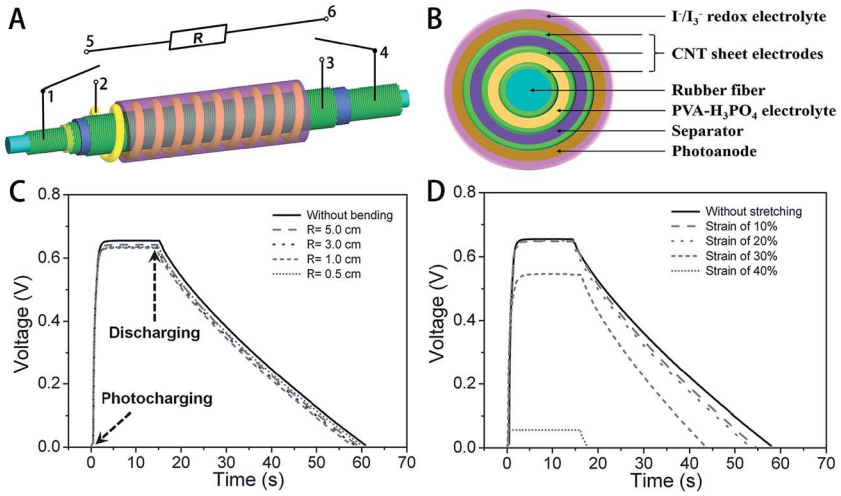

Fig. 4 (A) Schematic structure and (B) cross-sectional view of the coaxial energy fiber with energy conversion in the sheath and energy storage in the core. Photocharging–discharging processes of the energy fiber under (C) bent and (D) stretched conditions. The photocharging was carried out using a solar simulator at full-sun intensity (100 mW cm^{-2}). The galvanostatic discharging was conducted at a current density of 0.1 A g^{-1} using an electrochemical station. Redrawn from ref. 88.

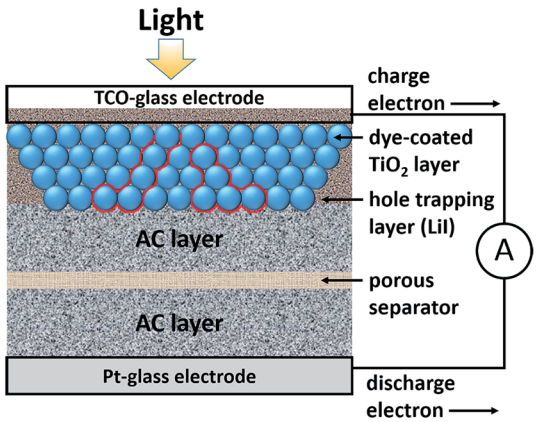

Fig. 5 Schematic illustration of two-electrode based SEES with integrated photoelectric and storage functions. Redrawn from ref. 97.

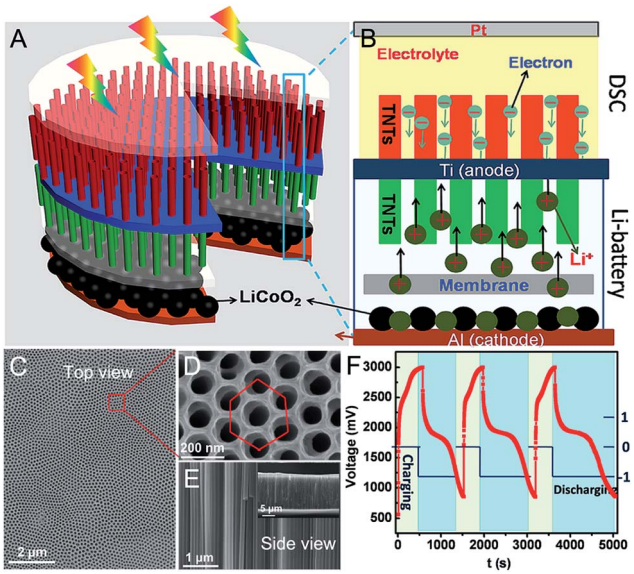

Fig. 6 (A) Design and (B) working principle of the power pack based on double-sided TiO_2 NT arrays. Top-view at (C) lower and (D) higher magnitude, and (E) side-view SEM images of vertically oriented anodized TiO_2 NT arrays fabricated on Ti foil at 50 V for 3 h. (F) Photocharging–discharging curves of the power pack. The device was discharged at a current of 100 μA and the light illumination was 100 mW cm^{-2}. Reprinted with permission from ref. 102. Copyright (2012) American Chemical Society.

energy without any intermediate processes. An external circuit is required for module I and therefore energy loss from electrical resistance is expected. Yet the advantage of module I is that it is applicable to all the energy conversion technologies, and is the most common type for SEESs. Modules II and III are two relatively new modules that require no external circuits, and thus have received ever increasing attention recently. Nevertheless, modules II and III may apply to only some specific energy conversion technologies due to the unique working principle of the energy conversion technology and/or difficulty in integrating the energy conversion and storage processes.

This review paper provides an overview of recent advancements in SEESs where EESs (mainly LIBs and SCs) are integrated with various energy conversion technologies with an emphasis on state-of-art organic solar cells, NGs, and HCs. SEESs for small-scale applications, *e.g.* portable & personal electronics, are mainly discussed herein considering the complexity and relatively high cost of the fabrication process of the device at the moment. First, organic solar cells including dye-sensitized solar cells (DSCs) & polymer solar cells (PSCs) and their applications for SEESs are presented. Secondly, three types of NGs, *i.e.* piezoelectric, triboelectric, and pyroelectric NGs are introduced, followed by highlights in the development

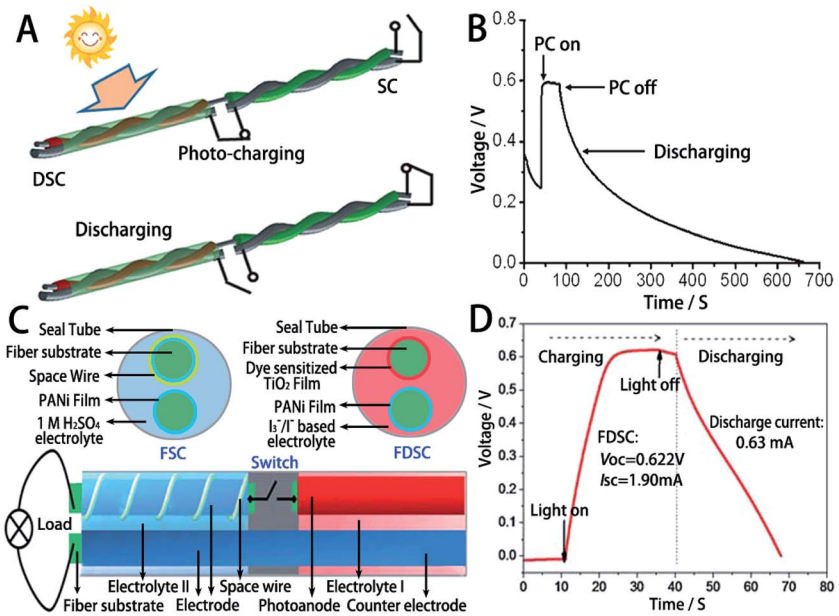

Fig. 7 (A) Schematic illustration of the integrated wire-shaped device for photoelectric conversion and energy storage using Ti as the integration platform, and (B) the corresponding photocharging–discharging curve (the discharging current is 0.1 μA);[106] (C) structural schematic of the integrated power fiber using PANi-SS as the integration platform and the sectional structure of the FDSC and the FSC, and (D) the corresponding photocharging–discharging curve.[107] The light illumination was 100 mW cm^{-2} for both devices. Redrawn from ref. 106.

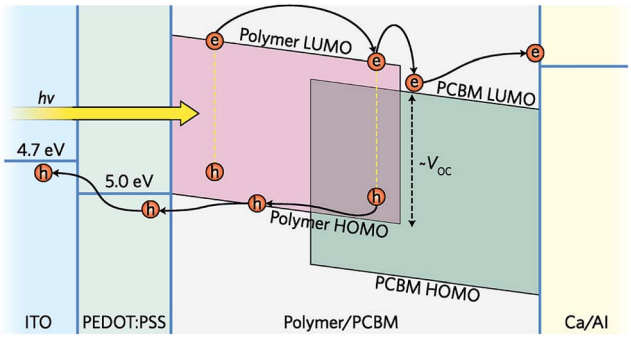

Fig. 8 Schematic energy diagram and working principles of polymer–fullerene-based PSCs. Redrawn from ref. 114.

of NG-powered SEESs. Thirdly, advances in HCs and their corresponding SEESs are discussed. Finally, future challenges and perspectives of SEESs are analyzed.

2. SEESs powered by different energy conversion technologies

2.1 Solar cell technology

Sunlight is recognized as a green and fully renewable energy source for the next-generation due to its abundance and negligible environmental issues. The energy can be scavenged *via* solar cell technologies, which directly convert sunlight into electricity.[49–54] High cost and complicated production processes associated with traditional silicon-based solar cells greatly limit their practical applications. In pursuit of low-cost solar cells over the last three decades, organic solar cells such as DSCs[55–59] and PSCs[60,61] have become research hotspots, and have both also been widely studied for SEES applications. No rectifiers are needed since only direct current (DC) signals are produced by DSCs and PSCs.

2.1.1 Dye-sensitized solar cells (DSCs). DSCs have received intense interest as a low-cost solar cell technology since their

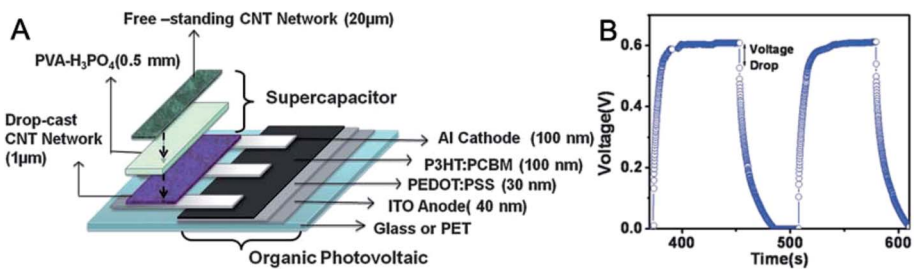

Fig. 9 (A) Schematic representation of and (B) photocharging–discharging curve of a PSC fabricated using the layer-by-layer approach. The light illumination was 100 mW cm^{-2}.[115]

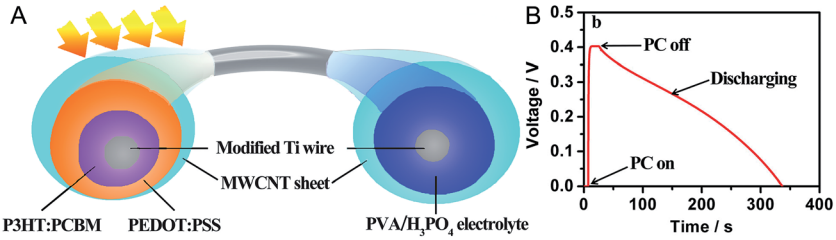

Fig. 10 (A) Schematic illustration of the structure of an all-solid-state, coaxial, and integrated fiber device (left: PSC; right: SC). (B) Photo-charging–discharging curve at a discharging current of 0.1 μA. The light illumination was 100 mW cm^{-2}. Redrawn from ref. 116.

first report in 1991.[62] In terms of conversion efficiency ($\eta_{conversion}$, refers to the ratio of the output maximum power by the solar cell to the input power, eqn (2.1)) and fabrication procedures, DSCs are believed to be one of the most promising alternatives to silicon solar cells.

$$\eta_{conversion} = \frac{FF \times V_{oc} \times J_{sc}}{P_{in}} \quad (2.1)$$

where FF, V_{oc}, J_{sc}, and P_{in} correspond to the fill factor, open-circuit voltage, short-circuit current density, and incident light power density, respectively. A typical DSC (Fig. 3A) consists of a transparent photoanode (*e.g.* fluorine-doped tin oxide, FTO, with a sintered mesoporous oxide, typically an anatase-phase TiO_2 layer, sensitized with organometallic dye molecules), an electrolyte containing a redox mediator (usually I^-/I_3^-) in an organic solvent, and a platinum (Pt) cathode. Sometimes, a compact film made of semiconductive materials (*e.g.* TiO_2) between the interface of the FTO and the porous TiO_2 is introduced as a block layer to inhibit charge recombination between the FTO substrate and the electrolyte, which otherwise causes a loss of photocurrent and therefore reduces the photovoltaic performance.[63,64]

A simplified energy diagram of how a DSC performs is presented in Fig. 3B. When exposed to sunlight, a photon is absorbed by the dye, exciting an electron (I). Then the electron is injected by the excited dye into the conduction band (CB) of TiO_2 (II) and diffuses to the current collector (III). The electron performs work and then flows to the cathode *via* an external circuit (IV). I_3^- is reduced to I^- in the electrolyte by receiving an electron transferred from the Pt counter electrode (V). The oxidized dye receives an electron from I^- and is regenerated to a neutral state (VI).

So far, the highest $\eta_{conversion}$ reported for a DSC is 14.3% using TiO_2 in the liquid electrolyte.[67] Photoanodes, *i.e.* semiconducting metal oxides like TiO_2, SnO_2, ZnO, NbO_5 and $SrTiO_3$, are considered to play a critical role in determining the performance of DSCs since they serve for both the collection and transportation of photo-excited electrons from the dye to the external electric circuit.[68,69] Endeavors to improve the $\eta_{conversion}$ have led to enormous research efforts to optimize the band gap, morphology, composition and thickness of the photoanode metal oxides.[70] Meanwhile, solid state DSCs (s-DSCs) have also been developed using hole-transport materials (HTMs) including organic (small molecules[71] or p-type conducting polymers[72]) or inorganic p-type semiconductors,[73] considering durability problems as well as electrode corrosion and electrolyte leakage arising from the use of organic liquid electrolytes. To date, the most commonly used HTM in s-DSCs is 2,2,7,7-tetrakis-(*N*,*N*-di-*p*-methoxyphenylamine)-9,9-spirobifluorene (spiro-OMeTAD),[74] but the tedious synthesis procedure and the high cost hinder its large scale application for commercial photovoltaics. Besides, the cell efficiencies of s-DSCs are usually much lower compared to those of their liquid counterparts; the record high $\eta_{conversion}$ of s-DSCs is 7.7% using spiro-OMeTAD doped with 1,1,2,2-tetrachloroethane,[75] whereas liquid DSCs with $\eta_{conversion}$ values approaching 15% are known. The general problem of HTMs in s-DSCs is believed to be poor filling of the nanoporous TiO_2 layer that interrupts the hole-conducting path between HTMs and the dye molecules adsorbed on TiO_2, as well as the low electrical conductivity of HTMs. To overcome these problems occurring in the s-DSCs, quasi-solid electrolytes or gel electrolytes prepared by immobilizing the liquid electrolyte using a low-molecular-mass organogelator (LMOG) have been developed.[76] These gel electrolytes exhibit higher ionic conductivity and better pore filling and penetration of the TiO_2 film. The highest $\eta_{conversion}$ achieved is 9.61% employing *N*,*N*′-1,5-pentanediylbis-dodecanamide as a LMOG in conjunction with a TiO_2 photoanode.[77] However, the stability of the quasi-solid electrolyte needs to be improved because the gelation is thermally reversible and the electrolyte returns back to a sol above the sol–gel transition temperature.[78]

To apply DSCs for SEESs applications, the most straightforward way is to simply connect two units that work independently in series *via* the external circuit (module I, see Fig. 2A).[79] The advantage of this setup lies in its simplicity, easy fabrication process, and low cost. Unfortunately, this configuration is usually space consuming due to the external connection system and has limited practical applications. More compact, more efficient and portable SEESs are therefore preferred. To this end, the development of fiber-shaped power packs, promoted by advancements in fiber-shaped energy conversion[80–83] and fiber-shaped storage devices,[84–86] has recently gained ever increasing attention. Compared with traditional two-dimensional energy devices, fiber-shaped energy packs feature unique one-dimensional wire structures with micro-scale diameters. They can be woven by conventional textile technologies and are expected to find promising applications in wearable devices and smart textiles.[87] Robust elastic electrodes are the key to maintaining the performance of fiber-shaped SEESs during the

Table 1 Structure details and key parameters of SEESs powered by DSCs and PSCs in the published papers[a]

SEESs module	Shape of SEESs	Energy conversion unit	Energy storage unit	V_{oc} (V)	J_{sc} (mA cm^{-2})	V_{max} (V)	Charging time	C_s	E	P	$\eta_{conversion}$	$\eta_{storage}$	$\eta_{overall}$	Ref.
I	Fiber	Liquid DSC, photoanode: TiO_2 NTs on Ti fiber; cathode: aligned CNT sheet	Symmetric solid SC based on aligned CNT sheet	0.68	14.31	0.65	Less than 1 s				6.47%		1.83%	88
II (*via* Pt sheet)	Planar	Liquid DSC, photoanode: TiO_2 nanoparticles on FTO glass; cathode: Pt sheet	Symmetric liquid SC based on PProDOT-Et_2			0.75		0.39 F cm^{-2}	22 μW h cm^{-2}	0.6 mW cm^{-2}			0.6%	89
II (*via* Pt sheet)	Planar	Liquid DSC, photoanode: TiO_2 particles on ITO coated with poly(ethylene naphthalate); cathode: Pt sheet	Symmetric liquid SC based on PEDOT	0.74	8.38	0.69		0.52 F cm^{-2}			4.37%			90
II (*via* Ag foil)	Planar	Solid state DSC, photoanode: TiO_2 on FTO deposited with a blocking layer of TiO_2; cathode: Ag layer	Symmetric liquid SC based on $RuO_x(OH)_y$ on carbon paper	~0.9	5	0.884	800 s	3.26 F cm^{-2}	0.17 mW h cm^{-2}	0.34 mW cm^{-2}	3%		0.8%	98
II (*via* silicon wafer)	Planar	Liquid DSC, photoanode: mesoporous TiO_2 nanoparticles on FTO glass; cathode: carbonized porous silicon wafer	Symmetric solid SC based on carbonized porous silicon wafer	0.68	11.5	0.6	1.2		0.17 μW h cm^{-2} (when V_{max} is 0.64 V)	22 μW cm^{-2} (when V_{max} is 0.64 V)	4.8%		2.1%	100
II (*via* Ni foil)	Planar	Liquid DSC, photoanode: TiO_2 particles on FTO; cathode: PEDOT coated Ni foil	Asymmetric liquid SC, anode: active carbon; cathode: Ni(Co)O_x on Ni foil	0.8	8.5	0.8	500 s	32 F g^{-1}	2.3 W h kg^{-1}	31 W kg^{-1}	4.9%		0.6%	101
II (*via* Ti sheet)	Planar	Liquid DSC, photoanode: TiO_2 NTs arrays on Ti; cathode: Pt	Liquid LIB, anode: TiO_2 NT arrays; cathode: $LiCoO_2$	3.39 (tandem DSCs)	1.01	2.996	Less in 8 min					41%	0.82%	102
II (*via* Ti sheet)	Planar	Liquid DSC, photoanode: TiO_2 NTs arrays on Ti; cathode: Pt	Symmetric liquid SC based on TiO_2 NTs arrays treated with	0.63	9.03	0.61	1 s	1.289 mF cm^{-2}	0.67 μW h cm^{-2}		3.17%	51.60%	1.64%	103

Table 1 (*Contd.*)

SEESs module	Shape of SEESs	Energy conversion unit	Energy storage unit	V_{oc} (V)	J_{sc} (mA cm^{-2})	V_{max} (V)	Charging time	C_s	E	P	$\eta_{conversion}$	$\eta_{storage}$	$\eta_{overall}$	Ref.
			hydrogen plasma											
II (*via* Ti wire)	Twisted fiber	Liquid DSC, photoanode: aligned TiO_2 NTs on Ti wire; cathode: CNTs fiber	Asymmetric solid SC, anode: CNTs fiber; cathode: aligned TiO_2 NTs	0.68	8.60	0.6		0.6 mF cm^{-2}	0.15 μW h cm^{-2}		2.2%	68.4%	1.5%	106
II (*via* a shared electrode)	Fiber	Liquid DSC, photoanode: TiO_2 nanoparticles on Ti wire; cathode: PANI coated stainless steel	Symmetric liquid SC based on PANI coated stainless steel	0.622	9.89	0.566					4.56%	46%	2.1%	107
II (*via* CNT)	Fiber	PSC, photoanode: P3HT:PCBM coated PEDOT/PSS-modified ITO glass; cathode: Al	Asymmetric solid SC, anode: free-standing CNTs network; cathode: drop-cast CNT network	0.6				28 F g^{-1}			3.39%			115
II (*via* Ti wire)	Fiber	PSC, photoanode: P3HT:PCBM coated PEDOT/PSS-modified MWNT sheets; cathode: TiO_2 modified Ti wire	Asymmetric solid SC, anode: MWNT sheets; cathode: TiO_2 modified Ti wire			~0.4		0.077 mF cm^{-1}	0.16 μW h cm^{-2}			65.6%	0.82%	116

[a] Note: the light illumination of the photocharging for the listed published papers is 100 mW cm^{-2}; PProDOT-Et_2 and PEDOT are short for poly(3,3-diethyl-3,4-dihydro-2*H*-thieno-[3,4-*b*][1,4]dioxepine) and poly(3,4-ethylenedioxythiophene), respectively.

bending and stretching process. Using aligned CNT sheets obtained from chemical vapor deposition (CVD), Yang *et al.*[88] designed an energy fiber with a coaxial structure where solar energy was converted into electric energy in the sheath and stored by the SC in the core (Fig. 4A). A cross-sectional illustration is provided to elucidate its structure (Fig. 4B). By connecting the photoanode (#2, helical Ti fiber with perpendicularly grown TiO_2 nanotubes) and the cathode (#3, aligned CNT sheets) of the outer photoelectrical-conversion unit to electrodes (#1 and #4, aligned CNT sheets with the same thickness) of the inner energy storage unit, the electricity converted from the DSC could be stored in the SC (photocharging process). The maximum charging voltage (V_{max}) and the current density (or charging rate) during the photocharging process are determined by the V_{oc} and J_{sc} of the solar cells, respectively.[89,90] The DSC herein exhibited a V_{oc} of 0.68 V and a J_{sc} of 14.31 mA cm^{-2}, and was able to fully charge the SC to 0.65 V within 1 s; then the fully charged SC could supply electrical energy for 41 s at a current density of 0.1 A g^{-1} (discharging process, where electrodes #1 and #4 are connected to electrodes #5 and #6, respectively). To study the potential applications for wearable electronics, the photocharging–discharging behavior of the energy fiber was investigated under bent and stretched conditions (Fig. 4C and D). The performance remained largely unaffected by bending at radii of curvature ranging from 5 to 0.5 cm; severe degradation occurred when the fiber was stretched beyond 40%.

Key parameters to evaluate the performance of SCs including specific capacitance (C_s), energy density (E) and power density (P) based on mass, length, area, or volume are also applicable

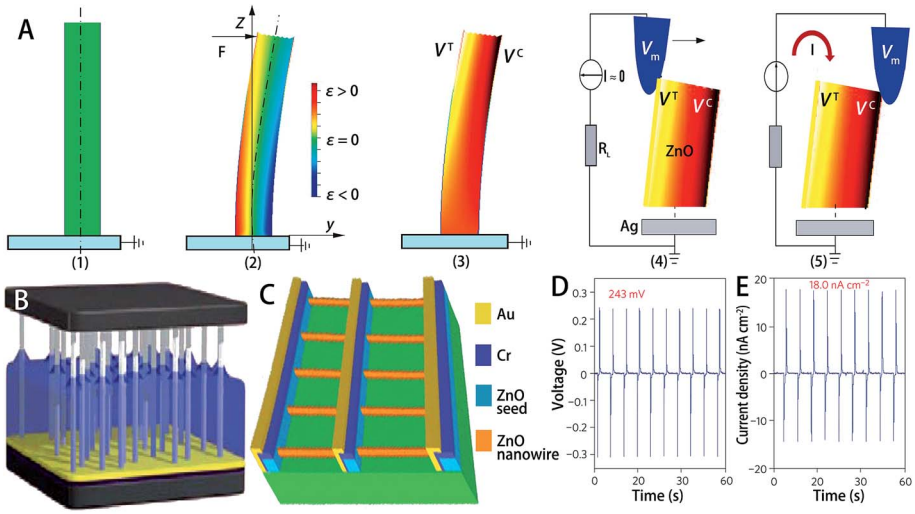

Fig. 11 (A) The working principle of a PiENG prototype to generate electricity by deforming a ZnO NW using a conductive AFM tip.[120] Schematics of (B) VINGs and (C) LINGs and their output current and voltage, and the output (D) potential and (E) current density produced by three serially-connected VINGs.[124] Redrawn from ref. 120 and 124.

for SEESs.[91,92] These parameters can be obtained using eqn (2.2)–(2.5) through galvanostatic discharging measurements when SC is disconnected from the DSC at the fully charged state and then connected to an electrochemical station.

$$C = \frac{i}{-\mathrm{d}V/\mathrm{d}t} \tag{2.2}$$

$$C_s = \frac{C}{M} \tag{2.3}$$

$$E = 0.5 \times C_s \times V^2 \tag{2.4}$$

$$P = \frac{E}{t_d} \tag{2.5}$$

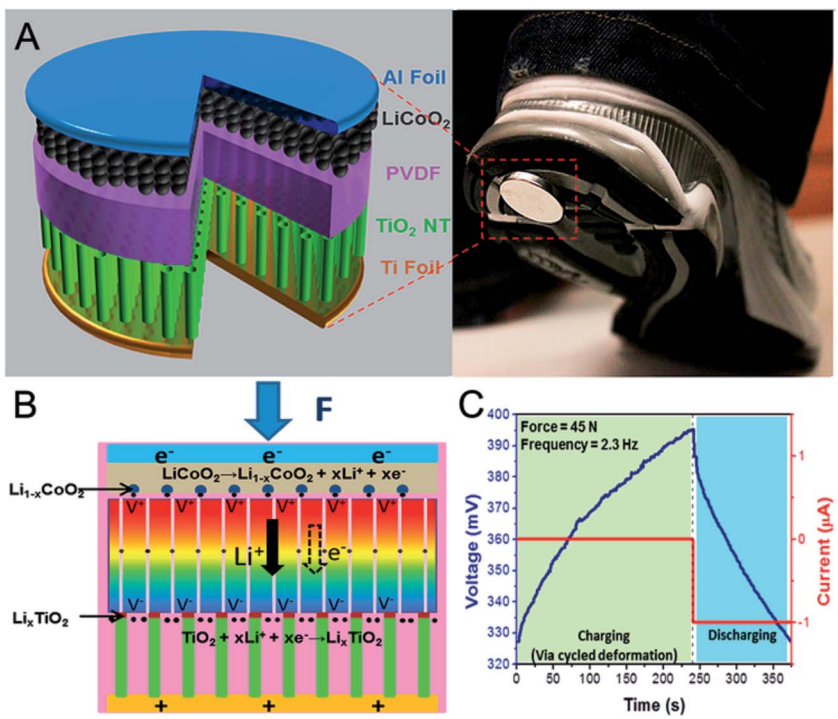

Fig. 12 (A) Schematic structure, (B) working mechanism, and (C) charging–discharging process (at a discharge current of 1 μA) of the SEES hybridizing a PiENG and a LIB sealed in a rigid stainless-steel 2016-coin-type cell. Reprinted with permission from ref. 133. Copyright (2012) American Chemical Society.

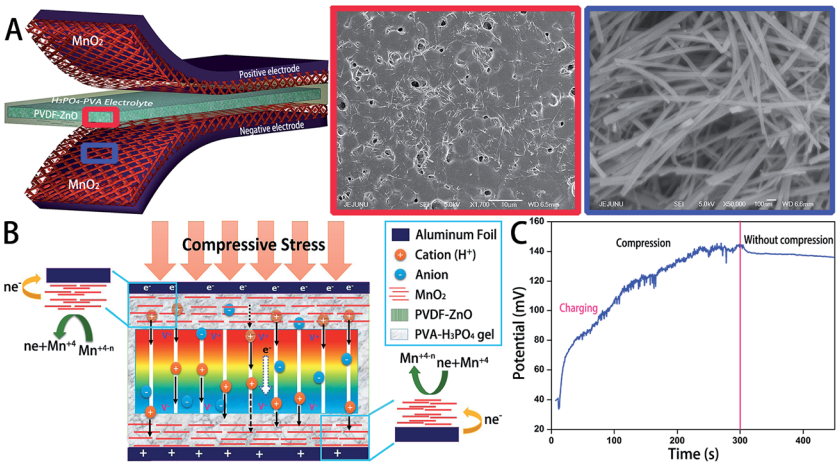

Fig. 13 (A) Schematic diagram of the device integrating a PiENG and a SC, and corresponding SEM images of piezoelectric PVDF–ZnO and MnO_2 used as SC electrode materials. (B) Working mechanism of the device. (C) Self-charging performance of SEES monitored using an electrochemical workstation under periodic compressive strain. Reprinted with permission from ref. 139. Copyright (2015) American Chemical Society.

where C is the capacitance, i is the discharge current, dV/dt is the slope of the discharge curve, C_s is the corresponding specific capacitance normalized by mass, length, area, or volume (M), E is the energy density, V is the operating voltage window (obtained from the discharge curve excluding the voltage drop), P is the power density, and t_d is the discharge time. Besides, the storage efficiency ($\eta_{storage}$) and the overall efficiency of energy conversion and storage ($\eta_{overall}$), defined by eqn (2.6) and (2.7), respectively,[88] are another two important parameters.

$$\eta_{storage} = \frac{E_{output}}{E_{input}} = \frac{0.5 \times C \times V^2}{P_{in} \times S \times t_c \times \eta_{conversion}} \quad (2.6)$$

$$\eta_{overall} = \eta_{conversion} \times \eta_{storage} \quad (2.7)$$

where E_{output} refers to the maximum output energy of the energy storage union, and E_{input}, P_{in}, S and t_c represent the maximum input light energy by the energy conversion union, the incident light power density, the area of the energy conversion union and the photocharging time, respectively. Due to the stable aligned CNT sheets and the coaxial structure, a maximum $\eta_{overall}$ of 1.83% was accomplished in this energy fiber with a photocharging time of 0.6 s.

As aforementioned, the connection between the energy conversion and storage sections *via* the external circuit in module I brings about higher electrical resistance and increases the overall size of the SEES. To avoid these problems, three-electrode modules consisting of a photoelectrode, an intermediate electrode (integration platform), and an external counter electrode were designed (module II, see Fig. 2B).[93–96] Interestingly, the three-electrode module was actually developed from

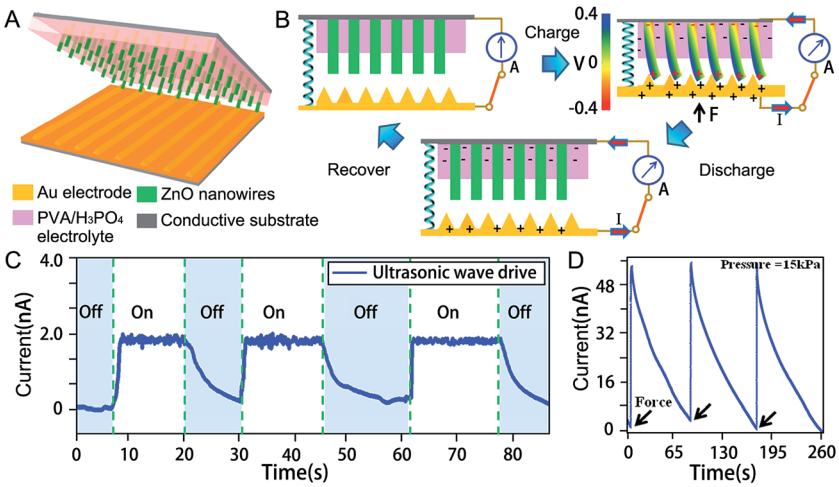

Fig. 14 (A) Schematic illustration of the structure and (B) working mechanism of the NEC with NG and SC dual functions. Close circuit current output of the NEC as the NEC is repeatedly input mechanical energy (C) by an ultrasonicator with a working frequency of 42 kHz and (D) under mechanical pulses of 15 kPa. Redrawn from ref. 141.

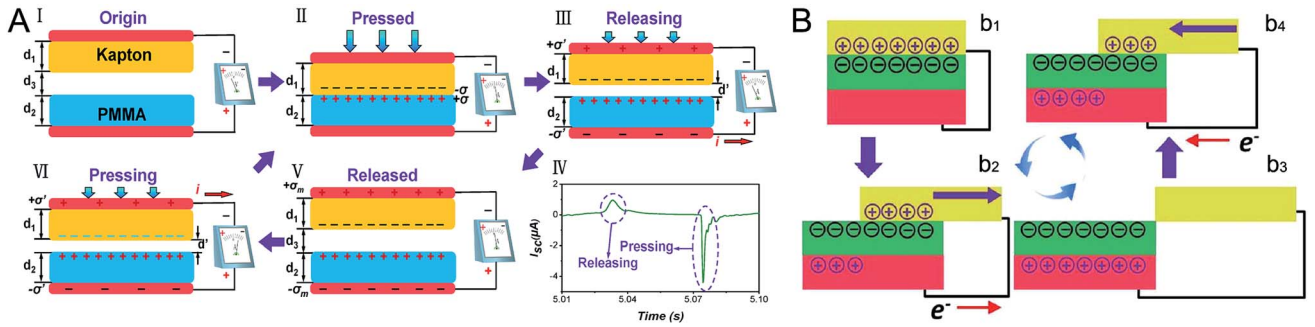

Fig. 15 Working principles of a TENG in (A) C-mode[147] using polymer films of Kapton and PMMA attached to aluminum as the electrodes and (B) S-mode using aluminum and PTFE-coated copper electrodes.[149] The aluminum, PTFE and copper are yellow, green, and red in color, respectively, in the S-mode TENG. Reprinted with permission from ref. 147 and 149. Copyright (2012) and (2013) American Chemical Society.

the two-electrode module (module III, see Fig. 2C) which was firstly proposed by Miyasaka *et al.*[97] The two-electrode prototype cell (Fig. 5) consisted of a light-absorbing electrode (photoelectrode, dye-adsorbed semiconductive TiO_2 nanoparticles further coated with a porous layer of activated carbon (AC)) and a counter electrode (a porous activated carbon layer). The operating principle was that the counter electrode functioned to collect electrons generated by the excited dye molecules, while the photoelectrode served to collect the corresponding holes. Due to the rather low energy conversion and charge storage efficiencies, an integration platform was later added to form a three-electrode module. DSC electrolyte regeneration occurs on one side of the integration platform whereas energy storage takes place on the other side. By comparison, the three-electrode modules exhibit a higher maximum voltage and therefore larger energy and power, a shorter complete charging time, a smaller voltage drop, and a higher $\eta_{overall}$.

In the three-electrode modules, the active electrode materials (*e.g.* conducting polymers or metal oxides) of the SCs are usually deposited on the shared platform *via* facile physical or chemical approaches. Pt or Ag was earlier employed to function as the integration platform between the DSC and the energy storage unit.[89,90,98,99] However, Pt and Ag are expensive, making the energy device costly. Metals (*e.g.* nickel, Ni) and semiconductors (*e.g.* silicon) which are much more abundant and cost effective, provide alternatives to Pt.[100,101] Guo *et al.*[102] fabricated a power pack comprising of tandem DSCs on the top and a LIB on the bottom sharing the Ti sheet substrate with TiO_2 nanotubes (NTs) grown on both sides (Fig. 6A). When exposed to sunlight, the excited electrons from the dye

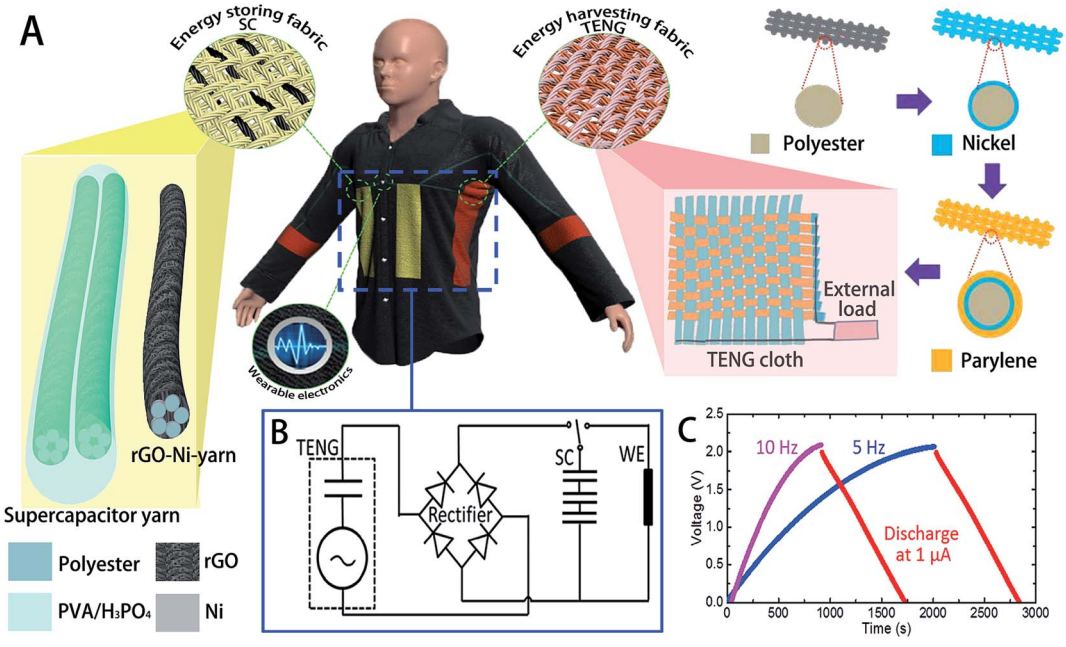

Fig. 16 (A) Scheme of a SEES integrating SC yarns as energy-storing fabrics, TENG cloth as energy-harvesting fabrics, and wearable electronics (WE, *e.g.* button sensors). (B) The corresponding equivalent circuit of the SEES. (C) The charge–discharge curves of three yarn SCs connected in series that are charged up by the TENG cloth at a motion frequency of 5 and 10 Hz, respectively. The discharge current is 1 μA. Redrawn from ref. 160 and 161.

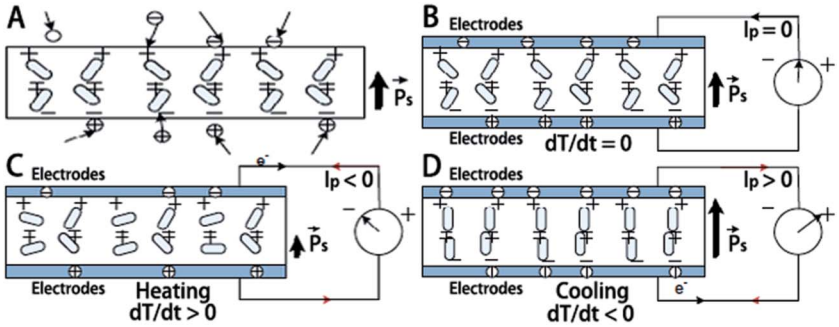

Fig. 17 (A) The pyroelectric material used as the dielectric material in a capacitor. Working principle of the PENG at (B) room, (C) increased and (D) reduced temperatures. Redrawn from ref. 169.

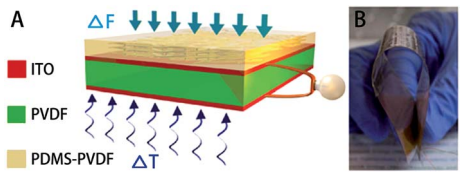

Fig. 18 (A) Schematic diagram and (B) photograph of a one-structure-based HC comprising of a triboelectric layer (PVDF nanowires–PDMS composite film) and piezoelectric–pyroelectric layers (a polarized PVDF film). Redrawn from ref. 180.

molecules would be injected into the CB of the TiO_2 NTs and transferred through the Ti foil to the anode of the LIB (TiO_2); the corresponding holes accumulated at the Pt electrode. The electrons from the DSCs reacted with the lithium ions at the LIB anode, inducing the chemical process $TiO_2 + xLi^+ + xe^- \rightarrow Li_xTiO_2$. Meanwhile, free electrons released from the reaction $LiCoO_2 \rightarrow Li_{1-x}CoO_2 + xLi^+ + xe^-$ at the cathode flowed back *via* the external circuit and combined with the holes at the Pt electrode of the DSC (Fig. 6B). Herein, the TiO_2 NTs were fabricated by electrochemically anodizing Ti foil. Top- and side-view SEM images are presented in Fig. 6C–E. To provide a high enough voltage to charge the LIB, three tandem DSCs, each of which was composed of two series-wound DSCs, were introduced. The resulting solar cell had a total V_{oc} of 3.39 V, nearly equivalent to an individual V_{oc} value of the tandem DSC, and charged the LIB to 2.996 V in around 8 min. The discharge capacity of the power pack was about 38.89 μA h under a discharge current density of 100 μA (Fig. 6F). The $\eta_{storage}$ and $\eta_{overall}$ values were mediocre at 41% and 0.82%, respectively. Similarly, Xu *et al.*[103] constructed a photo-supercapacitor (PSC) thin-film device consisting of a DSC and a SC built on bi-polar anodic TiO_2 NT arrays where the SC side was treated with selective hydrogen plasma. The hydrogen plasma treatment was capable of enhancing the capacitive performance of the SC, and therefore gave rise to an improved performance, with $\eta_{storage}$ and $\eta_{overall}$ values reaching 51.6% and 1.64%, respectively.

Even though these abovementioned planar-shaped SEESs are flexible, they still appear in relatively large size, which poses limitations on their potential applications for future electronic devices for which lightness and omni-directional flexibility are preferred.[104,105] For this purpose, wire-shaped energy packs with integrated functions of energy conversion and storage have been extensively explored in the past few years. Utilizing Ti wire as the common integration platform, Chen *et al.*[106] fabricated a twisted "energy wire" composed of one photoelectric conversion section and one energy storage section (Fig. 7A). The photocharging–discharging curve of the energy wire is shown in Fig. 7B, from which a $\eta_{storage}$ value of 68.4% and a maximum $\eta_{overall}$ value of 1.5% were calculated. Apart from Ti, other joint electrodes were explored to fabricate wire-shaped SEESs.[107] For example, polyaniline coated stainless steel (PANi-SS) was reported to function as the photocathode of the fiber-shaped DSC (FDSC) and also the electrode of the fiber-shaped SC (FSC, see Fig. 7C). This device demonstrated a $\eta_{storage}$ of 46% and a maximum $\eta_{overall}$ of 2.1% calculated from the photocharging–discharging curve in Fig. 7D. However, a liquid electrolyte was used in the device, which required that both the DSC and the SC be sealed separately, making the fabrication procedure very complex.

2.1.2 Polymer solar cells (PSCs). Polymer solar cells (PSCs) are another type of organic photovoltaic that have attracted significant interest in recent years. Differing from DSCs, PSCs are typically composed of photoactive materials sandwiched between two electrodes. They have advantages of easy fabrication, lower cost, flexibility of the organic molecules, and relatively high conversion efficiency.[108,109] Currently, high-efficiency PSCs are dominated by polymer–fullerene systems, where p-type conjugated polymers serving as electron donors and n-type fullerene derivatives serving as electron acceptors are constructed in a bulk heterojunction (BHJ) configuration functioning as the core component.[110,111] The BHJ configuration proves to be the most useful strategy that maximizes the internal donor–acceptor interfacial area and allows for an efficient charge separation. Significant progress has been made in BHJ PSCs since their inception in 1995.[112] The power conversion efficiency (PCE, *i.e.* $\eta_{conversion}$) of PSCs is now approaching 10%, indicating remarkable progress towards a promising future.

PSCs generally consist of three parts: an ITO positive electrode which is modified by poly(3,4-ethylenedioxythiophene)/poly(styrene sulfonate) (PEDOT/PSS), a low work function metal negative electrode, and a blend layer of a conjugated polymer donor and a fullerene derivative acceptor.[113] So far, the most

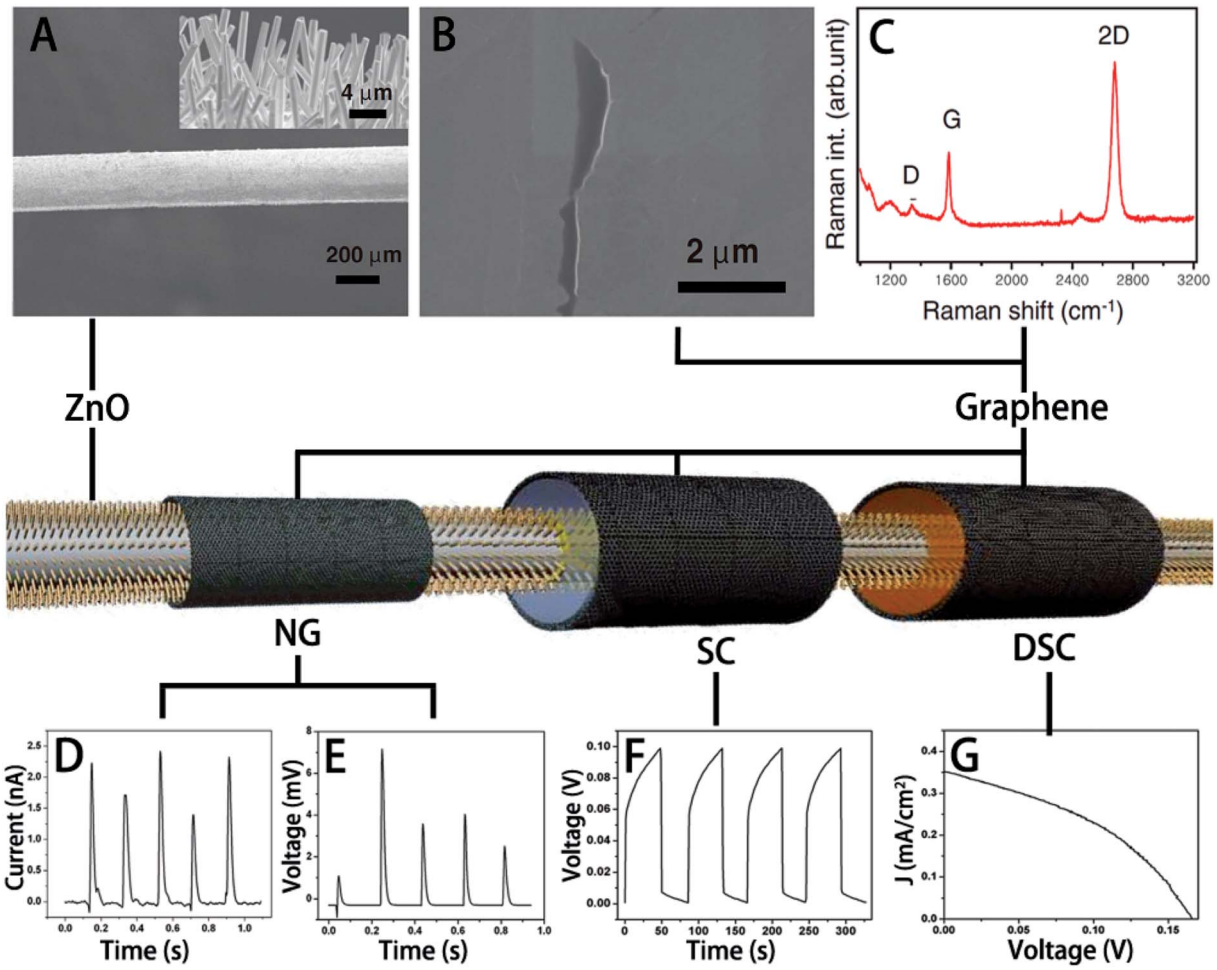

Fig. 19 Schematic of a fiber-based HC comprising of a PiENG, a DSC, and a SC, and their corresponding performance. ZnO NWs are grown on a flexible thin plastic wire coated with a thin Au film. Highly conductive and transparent graphene on Cu mesh was used as electrodes for each energy device. (A) SEM image of Au-coated plastic wire covered with ZnO NW arrays. (B) SEM image and (C) Raman spectra of graphene film. (D) Output current and (E) open-circuit potential of the PiENG. (F) Galvanostatic charge–discharge curve of the SC at 1 μA. (G) *J*–*V* curve of the DSC under one full-sun illumination. Redrawn from ref. 181.

prominent material system in BHJs is the mixture of poly(3-hexylthiophene):[6,6]-phenyl-C_{61}-butyric acid methyl ester (P3HT:PCBM). The working principle of PSCs is illustrated in Fig. 8.[114] In the first step, incident photons are absorbed by a conjugated polymer, creating excitons (bound electron–hole pairs). The produced excitons diffuse toward the donor/acceptor (D/A) interface where the electrons transfer from the LUMO of the donor to the LUMO of the acceptor to realize the charge separation. V_{oc}, the open-circuit voltage, is associated with the energy difference between the LUMO level of PCBM and the HOMO level of P3HT, and therefore provides a direct driving force for the charge separation. The photocurrent and the photovoltage are formed by the collected electrons and holes at the electrodes that transport along PCBM and the conjugated polymer, respectively, after the charge separation.

PSCs are promising for SEESs owing to their free of liquid electrolyte and great potentials to be fabricated onto large area and light-weight flexible substrates by solution processing at a lower cost. SCs are popular energy storage technologies to fabricate integrated OPV-SC modules due to their high power density, excellent cycle-stability, and high energy storage efficiency. A printable, all solid-state photo-supercapacitor (module II, see Fig. 2B) was reported using single-walled carbon nanotube (CNT) networks as a common integration platform between the PSC and the SC.[115] As illustrated in Fig. 9A, a CNT network that acted as an integration platform and the electrode of the SC was fabricated by the drop-casting of CNT solutions on top of the cathode (Al). The hybrid architecture had the advantages of low thickness (less than 0.6 mm) and light weight (less than 1 g). Meanwhile the internal resistance of the device was 43% lower than that of the device where the PSC and SC were connected by an external wire, as suggested by the much smaller voltage drop in the photocharging–discharging curve (Fig. 9B. The charge–discharge curve of a PSC and a SC that were connected externally using electrical wires with larger voltage drop, was not shown here).

To meet the ongoing push for electronics to be lightweight, smaller and weaveable, wire-shaped SEESs based on PSCs which

Table 2 Structure details and key parameters of SEESs powered by NGs and HCs in the published papers[a]

SEESs module	Shape of SEESs	Energy conversion unit	Energy storage unit	Charging time	C_s	Storage capability	Ref.
III	Planar	PiENG, piezoelectric building block: PVDF	Liquid LIB, anode: TiO_2 NT arrays on Ti foil; cathode: $LiCoO_2$	240 s (applied frequency: 2.3 Hz)		0.036 μA h	133
III	Planar	PiENG, piezoelectric building block: PVDF	Liquid LIB, anode: graphene; cathode: $LiCoO_2$	500 s (applied force: 34 N, 1 Hz)		0.266 μA h	134
III	Planar	PiENG, piezoelectric building block: PVDF–PZT	Liquid LIB, anode: MWNTs; cathode: $LiCoO_2$	240 s (applied force: 10 N, 1.5 Hz)		0.010 μA h	135
III	Planar	PiENG, piezoelectric building block: PVDF	Liquid LIB, anode: graphite; cathode: $LiCoO_2$	4 h (applied force: 70 N, 1.8 Hz)		4.5 μA h	136
III	Planar	PiENG, piezoelectric building block: β-phase PVDF	Liquid LIB, anode: graphite; cathode: $LiCoO_2$	200 s (input energy: 282 mJ, 1.0 Hz)		0.4 μA h	137
III	Planar	PiENG, piezoelectric building block: PVDF	Liquid LIB, anode: CuO/PVDF nanoarrays; cathode: $LiCoO_2$	240 s (applied force: 18 N, 1 Hz)		0.0247 μA h	138
III	Planar	PiENG, piezoelectric building block: PVDF–ZnO	Symmetric solid SC based on MnO_2 nanowires	120 s (applied force: 18.8 N)	0.26 F g^{-1}		139
I	Planar	TENG, electrodes: Ni-cloth belts and parylene-cloth belts	Symmetric solid SC based on rGO–Ni-yarns	2009 s (frequency: 5 Hz)			160
I	Planar	TENG, electrodes: Ni-cloth belts and parylene-cloth belts	Liquid LIB, anode: $Li_4Ti_5O_{12}$; cathode: $LiFePO_4$	14 h (frequency: 0.7 Hz)		4.4 mA h m^{-2}	161
II (*via* gold coated PMMA fiber)	Fiber	PiENG (building block: ZnO NW); DSC (photoanode: ZnO NW; cathode: graphene)	Asymmetric solid SC, anode: ZnO NW; cathode: graphene				181

[a] Note: PZT refers to lead zirconate titanate; PMMA is short for polymethyl methacrylate.

can be scaled up for practical applications by well-established textile technologies have been investigated. Zhang *et al.*[116] reported an all-solid-state, flexible "energy fiber" (module II, see Fig. 2B) that had efficient integrated functions of photovoltaic conversion and energy storage (Fig. 10A). The radial direction facilitated efficient charge generation and transportation in the PSC part and at the same time, the coaxial structure provided a high effective contact area for fast charge transportation in the SC part. Compared to the structures of two twisted fiber electrodes, this coaxial structure exhibited less electrical resistance and higher durability. Unfortunately, the maximum $\eta_{overall}$ was rather low, around 0.8% provided by the discharging curve in Fig. 10B. The insufficient V_{oc} of PSCs caused by the low PCE (hovering in the 6% range for BHJ PSCs) brought about a mismatch between the storage capability of the energy storage units and the energy generated by the PSC, and therefore led to unsatisfying $\eta_{overall}$. Even though the problem might be solved by connecting several PSCs in series, there is no doubt that doing so results in additional undesirable volume and size. Thus, it is imperative to increase the PCE *via* the new design and synthesis of high-efficiency conjugated polymer donor and fullerene derivative acceptor photovoltaic materials in the future.

Table 1 gives structure details (*i.e.* module, shape, energy conversion and storage components) and the corresponding parameters (V_{oc} and J_{sc} of the energy conversion unit and V_{max}, C_s, E, P, $\eta_{storage}$ and $\eta_{overall}$ of DSCs- and PSCs-powered SEESs). It is obvious that remarkable energy loss occurs in both the energy conversion and storage processes from the low values of $\eta_{conversion}$ and $\eta_{storage}$, especially in the energy conversion process. Since $\eta_{overall}$ is the product of $\eta_{conversion}$ and $\eta_{storage}$ (eqn (2.7)), advances in materials science and device design to enhance both $\eta_{conversion}$ of the energy conversion union and $\eta_{storage}$ of the energy storage union are key to improve the overall performance of SEESs. Besides, standard approaches to study SEESs need to be well established and the complete data need to be provided in the published papers to better determine the merits of the different results.

2.2 Nanogenerators (NGs) for harvesting mechanical/thermal energy

A nanogenerator (NG) is a new concept that harvests micro- and nano-scale mechanical/thermal energy from the ambient environment. Based on the energy harvesting approach, NGs can be classified into three categories: piezoelectric, triboelectric, and pyroelectric.[117] The first two convert mechanical energy into electricity whereas the third harvests thermal energy from a time-dependent temperature fluctuation. NGs have advantages of both high energy density and efficiency, a longer life time, and lower cost. Nevertheless, NGs can output only instantaneous power, and therefore usually need to be coupled with EES systems to extend their application scope.

2.2.1 Piezoelectric nanogenerators (PiENGs). PiENGs most of time refer to energy harvesting devices that convert external kinetic energy into electrical energy based on the coupled piezoelectric and semiconducting properties of nano-structured piezoelectric materials.[118,119] The first PiENG prototype that successfully converted mechanical energy into electricity using a single ZnO nanowire (NW) was demonstrated in 2006

(Fig. 11).[120] A piezoelectric potential across the NW was created due to the relative displacement of the Zn^{2+} cations with respect to the O^{2-} anions in the wurtzite crystal structure when a deformation was made by an atomic force microscope (AFM) tip. The stretched side exhibited a positive potential of V_T and the compressed side a negative potential of V_c (Fig. $11A_{1-3}$), assuming that the electrode at the NW's base was grounded. If the AFM platinum metal tip touched the NW's stretched side, the metal tip–ZnO interface was negatively biased since the value of ΔV was negative ($\Delta V = V_m - V_T < 0$, for the potential of the metal V_m was nearly zero, see Fig. $11A_4$). In this case, the platinum metal–ZnO semiconductor interface formed a reverse-biased Schottky diode and almost no current flow occurred (a Schottky diode behaves like a one-way gate, only allowing the current to flow from the direction of the metal to the semiconductor). The platinum metal tip–ZnO interface was positively biased if the AFM tip contacted the NW's compressed side since ΔV was positive ($\Delta V = V_m - V_c > 0$, Fig. $11A_5$). In this case, the metal semiconductor interface was a positively biased Schottky diode, and it produced an electrical current pulse resulting from a potential ΔV-driven flow of electrons from the semiconductor NW to the metal tip. Utilizing this approach, PiENGs outputting DC electric signals were developed based on aligned NWs that were covered by a zig-zag top electrode driven by an ultrasonic wave.[121] Yet the concerns of output stability, mechanical robustness, lifetime and environmental adaptability arose for this type of PiENGs. To address these problems, alternative current (AC) PiENGs were later designed from vertically or laterally aligned ZnO nanowire arrays with both ends firmly attached to metal electrodes.[122,123] Typical configurations of AC PiENGs are vertical nanowire array integrated nanogenerators (VINGs, see Fig. 11B) and lateral-nanowire-array integrated nanogenerators (LINGs, see Fig. 11C). To create a piezoelectric potential along the ZnO NWs, a periodic and uniaxial strain at low-frequency is applied to the NWs with the aid of an external mechanical action.[124] Fig. 11D and E present the output potential and current produced by three serially-connected VINGs.

The building block is another key factor besides device design in determining the performance of PiENGs. Rapid development has been made in the synthesis of nanostructured piezoelectric building blocks, including wurtzite compounds (*e.g.* ZnO,[125] CdS[126] and GaN[127]) and ferroelectrics (*e.g.* $BaTiO_3$)[128] in different shapes, *i.e.* nanowires, nanoplates, nanobeams, nanofilms and nanoparticles. NGs employing traditional piezoelectric materials including lead-zirconate-titanate (PZT)[129] and flexible piezoelectric polymers such as poly(vinylidene fluoride) (PDVF)[130] have also been demonstrated. Up to now, ZnO NWs have attracted the most research interest among various one-dimensional building blocks. Meanwhile, development in the mechanical and electromechanical characterization of these building blocks using theoretical calculations (*e.g.* surface/interface theory[131] and nonlocal piezoelectricity theory[132]) and experimental characterization methods (*e.g.* high-resolution transmission electron microscopy, and atom probe tomography) have also advanced the design of high performance PiENGs.

PiENGs can be easily integrated with energy storage unions to fabricate SEESs (module III, see Fig. 2C) due to the dual piezoelectric properties and ionic conductivity of piezoelectric materials. A fundamental mechanism that directly hybridized the energy conversion using a PiENG and energy storage using a LIB into one step, *i.e.* where the mechanical energy is directly converted and simultaneously stored as electro-chemical energy without any intermediate processes, was first introduced in 2012.[133] The mechanism was demonstrated by an experimental design in which conventional the polyethylene (PE) separator for the LIB battery was replaced with a piezoelectric PVDF film (Fig. 12). The cell was sealed in a rigid stainless-steel 2016-coin-type cell with $LiCoO_2$/conductive carbon/binder mixtures on aluminum foil as the cathode and TiO_2 NTs grown on Ti foil as the anode (Fig. 12A). Driven by the piezoelectric potential across the PVDF film caused by an external compressive strain, Li^+ ions were transported from the cathode to the anode, and induced the charging process at the electrodes. This process was defined as a piezo-electrochemical process (Fig. 12B). The role the PVDF film played in this SEES was similar to a DC power supply, but rather than pump electrons from the positive electrode to the negative electrode through the external circuit occurring in a conventional charging process of a LIB, the PVDF film pumped Li^+ ions from the positive to the negative electrode within the cell to achieve the charging process. The voltage of the device increased from 327 to 395 mV in 240 s under a compressive force at a frequency of 2.3 Hz, and returned to 327 mV at a discharge current of 1 μA in about 130 s, from which a stored electric capacity of 0.036 μA h could be calculated (Fig. 12C). The self-charging effect (voltage difference due to the applied compressive force) was found to increase with increasing magnitude and frequency of the compressive force.

Since the first demonstration of the SEES prototype hybridizing a PiENG and a LIB, much work has been done to improve the performance of the device for practical applications, *e.g.* the replacement of rigid device structures and electrodes with flexible materials to enhance the conversion efficiency[134] and optimization of the composition[135] or pore structure[136,137] of the piezo-separator to enhance the piezoelectric output or to facilitate transportation of Li ions. Efforts have also been made to combine the anode material with PVDF to fabricate a piezo-anode, so that the piezoelectric field will be better utilized because the integrated device structure allows for more intimate contact and a larger interface area between the anode material and PVDF.[138]

Based on a similar piezo-electrochemical process, the first SEES consisting of a PiENG and a SC was constructed by sandwiching piezoelectric PVDF–ZnO as the separator between two layers of electrochemically active manganese oxide (MnO_2) NWs (Fig. 13A).[139] The gel electrolyte in the solid SC avoided undesirable problems (*e.g.* processing complexity, electrode corrosion, and electrolyte leakage) associated with liquid electrolytes in LIBs. Under an external compressive stress, *i.e.* palm impact, the PVDF film would be polarized due to the piezoelectric effect. The piezoelectric potential across the PVDF–ZnO separator drove the H^+ ions in the electrolyte to migrate through the separator toward the negative electrode, leading to

corresponding charging reactions at the two electrodes (Fig. 13B). The voltage of the device increased from 35 to 145 mV in 300 s under continuous palm impact (Fig. 13C). Mechanical deformation or vibration energies from the surroundings can be utilized to charge such SEESs, and this therefore provides a new idea to design innovative power sources for portable electronics.[140] The integrated device is reported to have a much more effective charging process than those setups connecting a PiENG and an energy storage union through external circuits. Yet, more work is required to clarify and acquire a fundamental understanding of this new piezo-electrochemical process. *In situ* measurements, *e.g.* X-ray diffraction (XRD) or X-ray photoelectron spectroscopy (XPS) may provide approaches for observation of the electrodes and identification of the internal mechanism of the electron transfer. Besides, investigation into the overall efficiency (consisting of the energy converting efficiency of the piezoelectric material and the energy storage efficiency of this mechanical-to-electrochemical process) of the device is also necessary for comparison with those SEESs using other energy conversion unions, *e.g.* solar cells.

Relying on a mechanism different from the piezo-electrochemical process, an interesting nano-energy cell (NEC) with PiENG and SC dual functions was reported recently.[141] This novel NEC consisted of a sandwiched structure including a conductive substrate electrode, vertically aligned piezoelectric ZnO NW arrays embedded in a H_3PO_4/PVA gel electrolyte, and a serrated shape opposite electrode coated with Au (Fig. 14). A flexible spacer was employed to separate the electrodes with a small space under strain-free states. The NEC produced a DC current functioning like a PiENG if a mechanical energy was input, and discharged like an SC when the energy input was shut down. The discharge time lasted more than 90 s after each single mechanical pulse shock, more than 400 times higher than that of a NG. This phenomenon was explained by the part the of charges retained in the electrolyte injected from the ZnO NWs when external forces were applied onto the NWs. Much higher energy conversion was accomplished in this NEC, over 10 times higher than that of the PiENG. This NEC proposes another new concept to design PiENGs-based SEESs. Nevertheless, further improvement of the device is necessary since wearing and increased contact resistance/instability may occur due to scrubbing and sliding between the serrated electrode and the nanowires.

2.2.2 Triboelectric nanogenerators (TENGs). Triboelectric nanogenerators (TENGs) are a second type of mechanical energy-scavenging device which have been newly developed.[142] The working principle of a TENG is based on a coupled effect of contact-electrification and electrostatic induction *via* two materials exhibiting significantly different tribo-polarities, with one easily able to gain electrons and the other one easily able to lose electrons. Although triboelectric-associated electrostatic phenomena are the most common phenomena in our daily life, sometimes even deemed detrimental for electronic systems, the first TENG to generate electricity by utilizing this ignored and wasted mechanical energy was not developed until 2012.[143] So far, two basic operating modes have been developed, namely contact mode (C-mode)[144] and sliding mode (S-mode),[145,146] to harvest ambient mechanical motions under different circumstances (Fig. 15). In the C-mode TENG, the working mechanism is depicted by the cycled electric potential difference (EPD) that is caused by the periodic separation and re-contact of two films with opposite triboelectric charges on the inner surfaces.[147] Polymer films of Kapton and PMMA (polymethyl methacrylate) with remarkably different tribo-polarities are used here to illustrate the working mechanism of a TENG (Fig. $15A_I$). By bending or pressing the device, charge transfer between the two films takes place due to the triboelectric effect, with the surface of Kapton positively charged and that of PMMA negatively charged (Fig. $15A_{II}$). The EPD across the top and bottom electrodes in the inner circuit begins to be established during the releasing process (Fig. $15A_{III}$). In order to screen the EPD, electron flow between the two electrodes (*i.e.* aluminum attached to the polymer films) occurs under short-circuit conditions, resulting in a current pulse (Fig. $15A_{IV}$). Once the deformation is fully released, positive and negative induced charges accumulate on the top and bottom electrodes, respectively (Fig. $15A_V$). The EPD that is induced by the triboelectric effect will be reduced to zero when the two films are in close contact, and therefore results in the flow back of the triboelectric-effect-induced charges, generating another instantaneous current in the opposite direction (Fig. $15A_{VI}$).

Different from C-mode TENGs, S-mode TENGs (Fig. 15B) are based on the in-plane sliding between two triboelectric layers that can slide smoothly one against the other in a lateral direction.[148] The working principle can be illustrated in an S-mode TENG consisting of an aluminum thin film functioning as both the electrode and the sliding layer, and polytetrafluoroethylene (PTFE) film serving as the other sliding layer with a copper electrode adhered beneath.[149] At a fully aligned position, similar to the process in C-mode TENGs, charge transfer occurs due to the triboelectric effect or contact electrification after the two layers are in intimate contact (Fig. $15b_1$). Once a relative displacement is applied parallel to the layers, triboelectric charges are not compensated at the displaced/mismatched areas, inducing a dipole polarization parallel to the displacement and an EPD will be created across the two electrodes. Under short-circuit conditions, free electrons from the copper to the aluminum electrode driven by the uncompensated negative triboelectric charges on PTFE will neutralize the positive triboelectric charges, leaving behind positive induced charges (Fig. $15b_2$). The positive triboelectric charges are supposedly to be completely balanced out by induced electrons when the displacement reaches a maximum (Fig. $15b_3$). The induced electrons would flow back to the copper electrode when the displacement is removed by a reciprocating force (Fig. $15b_4$), until the position is fully restored.

AC signals are produced in both C- and S-mode TENGs if the periodic mechanical deformation or displacement lasts. The electric output and efficiency of TENGs are mainly determined by two critical processes: charge separation and periodic separation/contact switching of the two charged plates.[150] The former can be obtained through the right choice of material match with the largest difference in capacity for gaining/losing electrons according to the triboelectric series, or through

modification of the surface morphology. A surface with more sophisticated structures is found to have a larger effective triboelectric effect and thus can generate more surface charges during the friction.[151] The current density for TENGs using PDMS film with pyramid patterns is found to be 5–6 times as high as its counterpart using unstructured films.[152] Effective separation/contact is mainly achieved *via* rational optimization of the TENG design. Arch-shaped TENGs or the introduction of springs were reported to facilitate separation–contact cycles.[144,153] Moreover, three-dimensional TENGs working in a hybridization of the C- and S-modes were also developed to better utilize ambient vibration energy in full space.[154]

Apart from the unprecedented output performance, the advantages of high efficiency, low-cost, environmental friendliness, universal availability, and versatility of the materials make TENGs the right choice to be integrated with fabric energy storage unions for SEESs applications to power wearable electronics (*e.g.* small healthcare electronics including heartbeat meters, pedometers and pulse meters) *via* scavenging the energy of daily human motions (Fig. 16A).[34,155] The core challenge for textile TENGs and LIBs or SCs has been the fabrication of lightweight, mechanically strong, and electrically conductive 1D yarns or fibers which can be readily incorporated into human wearable electronics with arbitrary shapes and high flexibility as building blocks.[156] To date, various strategies have been developed, *e.g.* continuous spinning of CNT yarns *via* electrospinning,[157] direct use of metal wires,[158] and conformal deposition of conductive materials onto conventional fabrics.[159] However, there might be some disadvantages with these approaches, for example, the high cost associated with electrospinning CNT yarns, the low conductivity of the dip-coated fabric yarns, and the heavy weight of metal wires. To overcome these shortcomings, Pu *et al.*[160] used low cost, flexible, and mechanically strong polyester fabric coated with Ni film to obtain light yet highly conductive 1D yarns (density: 2.1 mg cm^{-3}; length resistance: 1.48 Ω cm^{-1}). The yarns were then coated with reduced graphene oxide (rGO) to get rGO–Ni-yarns, from which a symmetric yarn SC was assembled. Meanwhile, polyester straps were coated firstly with Ni (Ni-cloth belts) and then with insulating parylene film to get parylene-cloth belts. Parylene-cloth belts as latitude lines and Ni-cloth belts as longitude lines were then woven to yield TENG-cloth, with all the Ni-cloth belts connected together by copper wire as one electrode, and all the parylene-cloth belts connected as the other. The light, soft, washable, breathable, stretchable textile TENGs for energy harvesting and textile SCs for energy storage were integrated into an individual textile (module I, see Fig. 2A) for wearable smart electronic applications. A rectifier, which can be designed into a logo or button due to its rigidity, was used to rectify the current to charge the SC yarns. The equivalent circuit of the SEES for wearable electronics is shown in Fig. 16B. In this way, human motion energy can be harvested by the TENG cloth in a contact–separation mode motion with a common cotton cloth and then stored in the textile SCs. By applying a vibration motor operating at about 5 Hz, the three serially-connected SC yarns can be charged to 2.1 V in 2009 s by the TENG cloth (Fig. 16C).

Currently the main challenge for SEESs based on TENGs is the low utilization of the electricity generated by the TENG, which is caused by the significant impedance mismatch between the TENG and the energy storage device. TENGs possess characteristics of high impedance (10^5 to 10^7 Ω),[162] several orders higher than those of SCs and LIBs (around 10^{-2} to 10^2 Ω). A transformer with appropriate design is reported to be effective in bridging the impedance gap between the TENG and the energy storage device. 72.4% power utilization efficiency between a TENG and a LIB was achieved with a transformer coil ratio of 36.7,[163] but more work is needed to integrate the circuit design into wearable and flexible textiles.

2.2.3 Pyroelectric nanogenerators (PyENGs). A pyroelectric nanogenerator (PyENG) is a device that converts external thermal energy into electrical energy based on the fact that the spontaneous polarization (dielectric constant) in certain anisotropic solids is temperature dependent.[164–166] It is well-known that thermal energy can be scavenged *via* a temperature difference across two ends of the device to drive the charge carriers to diffuse (the Seebeck effect);[167,168] nevertheless, the pyroelectric effect has to be the choice in an environment where the temperature is spatially uniform but time-dependent. The first PyENG was introduced in 2012.[164] By utilizing the heat energy otherwise wasted, this newly developed NG has promising applications for self-powered nano/micro devices, smart wearable systems, *etc.*

The working principle of PENGs is demonstrated in Fig. 17.[169] Pyroelectric materials are able to attract charged particles arising from the spontaneous polarization PS that is non-zero at room temperature (Fig. 17A). A charging process takes place in a short-circuit connection when the pyroelectric material serves as the dielectric material and is sandwiched between two plates of a capacitor. The charging of the capacitor continues until the charge is neutralized on the pyroelectric material surface (Fig. 17B). At increased temperatures across the capacitor, the dipoles within the pyroelectric material start to become randomized, resulting in both reduced PS and dielectric constant. A continuous current flow is expected in the external circuit if the temperature change across the capacitor lasts (Fig. 17C). If the temperature is reduced, the dipoles in the pyroelectric material realign again, giving rise to a current flow in the opposite direction (Fig. 17D). Therefore, AC signals will be generated in the external circuit under rapid temperature cycling across the capacitor. Both the magnitude of the AC signals and the energy conversion efficiency depend on the temperature change rate. Even though no SEESs based on a single PyENG have been reported yet, to our best knowledge, PyENGs are usually used in HCs-based driven SEESs (Section 2.3).

2.3 Hybrid cells for harvesting multiple types of energy

Hybrid cells (HCs) to concurrently harvest multiple types of energy have become a well-received approach in energy conversion technologies recently.[170,171] There are several reasons justifying the development of HCs. Firstly, the energy produced by an individual NG is relatively small and thereby still has

limited use as a supplementary energy source. HCs can improve the output performance to meet the demands of larger electronics and thus widen the practical applications of NGs. Secondly, the energy sources in our living environment are not available all the time, but are usually time- or climate-dependent. For instance, a solar cell depends on abundant sunshine while a mechanical energy-driven NG works if only sufficient mechanical movement or vibration is provided. On the contrary, a HC is capable of utilizing complementary energy sources around the clock whenever and wherever one or all of them is available. Thirdly, the energy can be more effectively scavenged using a HC. Take a TENG for example, a substantial amount of energy input is wasted through heat dissipation induced by friction, especially if a sliding motion at high frequency is applied; moreover, extra energy loss is generated from the work done by the necessary normal force applied on the contact surface. It is therefore highly desirable if the TENG is combined with a PyENG and a PiENG to harvest the thermal energy from the friction-induced temperature fluctuation and the mechanical energy from the small deformation of materials caused by the normal force, respectively.

The first HC was demonstrated in 2009, which consisted of a DSC and a PiENG that worked simultaneously and independently to scavenge solar energy and mechanical energy, respectively.[172] Later research was conducted to optimize the design of the HC[173] or to construct other structured HCs, for example, core–shell coaxially fiber-shaped HCs for remote/concealed locations.[174] Meanwhile, some other modes of HC have sprung up, such as a solar cell hybrid with a TENG,[175] a TENG with a PyENG,[176] a PiENG with a TENG,[177] or HCs consisting of a TENG, a PiENG and a PyENG, to name a few.[178]

A second type of HC was proposed using the same electrode with both pyroelectric and piezoelectric properties, and has gained significant attention recently. Materials such as ZnO, PZT, and PVDF can be utilized for this purpose to reduce both the size and the fabrication cost of HCs.[179] A highly stretchable PiENG–PyENG HC was reported using poly(vinylidenefluoride-*co*-trifluoroethylene) [P(VDF–TrFE)] as the pyroelectric and piezoelectric material which was spun-coated onto a micro-patterned PDMS–CNT composite to simultaneously harvest mechanical and thermal energy.[48] Relying on the piezoelectric, pyroelectric, and triboelectric properties of PVDF, a one-structure-based HC comprising of a triboelectric layer (PVDF nanowires–PDMS composite film) and piezoelectric–pyroelectric layers (a polarized PVDF film) was designed (Fig. 18).[180] This HC not only minimized the device but also was capable of coupling the advantages of NGs based on different mechanisms to accomplish high output performance.

The first prototype to integrate a HC with an energy storage system was proposed in 2011 which included a PiENG, a DSSC, and a SC built along one micro-size plastic fiber coated with Au (Fig. 19).[181] Radially grown ZnO nanowires (NWs, see Fig. 19A) on a Au substrate served to harvest mechanical energy in the NGs, and meanwhile acted as the core component of the DSC and the SC. Copper meshes covered with graphene (Fig. 19B and C) were carefully wrapped around the fiber to function as the other electrode for the PiENG, DSC, and the SC. In the PiENG, the ZnO NWs and the graphene formed a Schottky contact, and the maximum output current and open-circuit potential were 2 nA and 7 mV, respectively (Fig. 19D and E). In the case of the DSC, the J_{sc} and V_{oc} were determined to be 0.35 mA cm^{-2}, and 0.17 V, respectively (Fig. 19F). As for the SC, which consisted of a gel electrolyte sandwiched between ZnO NWs and graphene electrodes, a length capacitance of 0.025 mF cm^{-1} was achieved (Fig. 19G).

Considering the differences in both the output electric signals and the impedance of each type of NG, circuit design has to be considered in fabricating SEESs using HCs as energy harvesters.[179,182] For example, AC output electric signals are usually generated from PyENGs, PiENG, and TENGs while DC output signals are generally obtained from solar cells. On the other hand, each NG may output remarkably different voltages or currents. The V_{oc} of a TENG may be several hundreds of volts while a solar cell may have a V_{oc} within one volt. AC–DC converters (*e.g.* a rectifier), DC–DC converters, or transformers are therefore necessary to be included in the circuit to economically charge the energy storage devices.

Table 2 summarizes structure details and the corresponding parameters of SEESs powered by NGs and HCs. More complete data such as overall conversion efficiency is recommended to be provided in future published papers to better compare their performances.

3. Conclusions and perspectives

To summarize, SEESs have been proved to be an innovative approach to hybridizing energy conversion technologies with energy storage components. Wire-structured SEESs hold great promise for next-generation portable, wearable smart electronics when compared to their conventional planar-structured counterparts. Advances in SEESs powered by various energy conversion technologies with an emphasis on solar cells (*i.e.* DSCs and PSCs), NGs (*i.e.* PiENGs, TENGs, and PyENGs), and HCs are reviewed. In particular, HCs coupling multiple types of energy conversion technologies have been attracting increasing attention due to their capability to more effectively scavenge both small- and large-scale energy in a complementary manner around the clock. Even though significant progress has been made to date, future work is still required. Reducing the manufacturing cost and enhancing the overall efficiency are two key factors to extend the practical applications of SEESs. Devices relying on cost effective raw materials, requiring fewer steps for fabrication and simpler packaging are preferred.[100] Rational material selection and optimal device design to more effectively harvest and store the energy are critical to achieve improved overall efficiency, which currently remains around 2% arising from the low $\eta_{conversion}$ in the energy harvester and low $\eta_{storage}$ in the energy storage unit. Moreover, the approaches to assess the performance of the SEESs have not been well established or standardized yet; the related data provided in the literature is not complete, making it sometimes difficult for comparison between different research results.

Specifically, for each type of energy conversion technology, different work may be required. In the case of DSCs, a popular

approach to scavenging energy for SEESs due to the simpler circuit design and high conversion efficiency, more efforts are required to develop high performance solid- or quasi-solid-DSCs to replace currently ubiquitous liquid DSCs considering durability and safety concerns as well as the complexity of the sealing process. As for PSCs, which are free of liquid electrolyte and have advantages of being able to be fabricated into more compact and lighter weight devices, the challenge is to enhance the energy conversion efficiency, which can be accomplished *via* the synthesis of a high-efficiency conjugated polymer donor and a fullerene derivative acceptor that maximize the light harvesting (for example, to extend the light-harvesting region into the near-infrared), and optimization of the device design to minimize the loss-in-potential and to lower the overpotentials required to drive the electron transfer in the desired direction.[67] For SEESs based on NGs, more work in clarifying the new piezoelectrical process in PiENGs is needed to improve the overall efficiency. The impedance match between TENGs and energy storage unions is vital to achieve optimum device performance to power wearable electronics *via* scavenging the energy of daily human motions. In the HCs-powered SEESs, electrical design has to be considered to efficiently charge the energy storage devices.

Acknowledgements

The financial support from Tianjin Natural Science Foundation (20020), start-up fund of Tianjin University of Science and Technology (10276), and Youth Innovation Foundation of Tianjin University of Science and Technology (2015LG01 and 201510057069) is kindly acknowledged.

References

1 R. Mendelsohn, I. C. Prentice, O. Schmitz, B. Stocker, R. Buchkowski and B. Dawson, *Am. Econ. Rev.*, 2016, **106**, 612–614.
2 M. Höök and X. Tang, *Energy Policy*, 2013, **52**, 797–809.
3 C. O. Colpan and O. Kizilkan, *Int. J. Energy Res.*, 2016, **40**, 3.
4 N. Abas, A. Kalair and N. Khan, *Futures*, 2015, **69**, 31–49.
5 S. P. S. Badwal, S. S. Giddey, C. Munnings, A. I. Bhatt and A. F. Hollenkamp, *Front. Chem.*, 2014, **2**, 79.
6 Z. Yang, J. Zhang, M. C. W. Kintner-Meyer, X. Lu, D. Choi, J. P. Lemmon and J. Liu, *Chem. Rev.*, 2011, **111**, 3577–3613.
7 H. Ibrahim, A. Ilinca and J. Perron, *Renewable Sustainable Energy Rev.*, 2008, **12**, 1221–1250.
8 *Electrochemical technologies for energy storage and conversion*, ed. R.-S. Liu and L. Zhang, Wiley-VCH-Verl, Weinheim, 2012.
9 A. Poullikkas, *Renewable Sustainable Energy Rev.*, 2013, **27**, 778–788.
10 X. Luo, J. Wang, M. Dooner and J. Clarke, *Appl. Energy*, 2015, **137**, 511–536.
11 Z. Li, D. Young, K. Xiang, W. C. Carter and Y.-M. Chiang, *Adv. Energy Mater.*, 2013, **3**, 290–294.
12 X. Rui, W. Sun, C. Wu, Y. Yu and Q. Yan, *Adv. Mater.*, 2015, **27**, 6670–6676.
13 T. J. Carter, R. Mohtadi, T. S. Arthur, F. Mizuno, R. Zhang, S. Shirai and J. W. Kampf, *Angew. Chem., Int. Ed.*, 2014, **53**, 3173–3177.
14 B. Pan, J. Huang, Z. Feng, L. Zeng, M. He, L. Zhang, J. T. Vaughey, M. J. Bedzyk, P. Fenter, Z. Zhang, A. K. Burrell and C. Liao, *Adv. Energy Mater.*, 2016, **6**, 1600140–1600145.
15 M.-C. Lin, M. Gong, B. Lu, Y. Wu, D.-Y. Wang, M. Guan, M. Angell, C. Chen, J. Yang, B.-J. Hwang and H. Dai, *Nature*, 2015, **520**, 324–328.
16 N. Jayaprakash, S. K. Das and L. A. Archer, *Chem. Commun.*, 2011, **47**, 12610–12612.
17 P. Simon, Y. Gogotsi and B. Dunn, *Science*, 2014, **343**, 1210–1211.
18 *Lithium-ion batteries: science and technologies*, ed. M. Yoshio, R. J. Brodd and A. Kozawa, Springer, New York, 2009.
19 P. Simon and Y. Gogotsi, *Nat. Mater.*, 2008, **7**, 845–854.
20 H. Wei, H. Gu, J. Guo, S. Wei and Z. Guo, *ECS J. Solid State Sci. Technol.*, 2013, **2**, M3008–M3014.
21 H. Wei, H. Gu, J. Guo, S. Wei, J. Liu and Z. Guo, *J. Phys. Chem. C*, 2013, **117**, 13000–13010.
22 H. Wei, X. Yan, S. Wu, Z. Luo, S. Wei and Z. Guo, *J. Phys. Chem.C*, 2012, **116**, 25052–25064.
23 H. Wei, J. Zhu, S. Wu, S. Wei and Z. Guo, *Polymer*, 2013, **54**, 1820–1831.
24 H. Wei, D. Ding, X. Yan, J. Guo, L. Shao, H. Chen, L. Sun, H. A. Colorado, S. Wei and Z. Guo, *Electrochim. Acta*, 2014, **132**, 58–66.
25 Y. He, W. Chen, C. Gao, J. Zhou, X. Li and E. Xie, *Nanoscale*, 2013, **5**, 8799.
26 Z. Yu, L. Tetard, L. Zhai and J. Thomas, *Energy Environ. Sci.*, 2015, **8**, 702–730.
27 Y. Tang, Y. Zhang, W. Li, B. Ma and X. Chen, *Chem. Soc. Rev.*, 2015, **44**, 5926–5940.
28 H. Gu, Y.-E. Zhu, J. Yang, J. Wei and Z. Zhou, *ChemNanoMat*, 2016, **2**, 578–587.
29 F. Zhang, Y. Tang, H. Liu, H. Ji, C. Jiang, J. Zhang, X. Zhang and C.-S. Lee, *ACS Appl. Mater. Interfaces*, 2016, **8**, 4691–4699.
30 D. P. Dubal, O. Ayyad, V. Ruiz and P. Gómez-Romero, *Chem. Soc. Rev.*, 2015, **44**, 1777–1790.
31 J. B. Goodenough and K.-S. Park, *J. Am. Chem. Soc.*, 2013, **135**, 1167–1176.
32 M. B. Sassin, C. N. Chervin, D. R. Rolison and J. W. Long, *Acc. Chem. Res.*, 2013, **46**, 1062–1074.
33 S. Niu, X. Wang, F. Yi, Y. S. Zhou and Z. L. Wang, *Nat. Commun.*, 2015, **6**, 8975.
34 G. Zhu, P. Bai, J. Chen and Z. Lin Wang, *Nano Energy*, 2013, **2**, 688–692.
35 Z. Li, J. Chen, H. Guo, X. Fan, Z. Wen, M.-H. Yeh, C. Yu, X. Cao and Z. L. Wang, *Adv. Mater.*, 2016, **28**, 2983–2991.
36 J. Luo, F. R. Fan, T. Jiang, Z. Wang, W. Tang, C. Zhang, M. Liu, G. Cao and Z. L. Wang, *Nano Res.*, 2015, **8**, 3934–3943.
37 J. Wang, Z. Wen, Y. Zi, P. Zhou, J. Lin, H. Guo, Y. Xu and Z. L. Wang, *Adv. Funct. Mater.*, 2016, **26**, 1070–1076.

38 H. Sun, Y. Jiang, L. Qiu, X. You, J. Yang, X. Fu, P. Chen, G. Guan, Z. Yang, X. Sun and H. Peng, *J. Mater. Chem. A*, 2015, **3**, 14977–14984.
39 J. Xu, Y. Chen and L. Dai, *Nat. Commun.*, 2015, **6**, 8103.
40 X. Xu, S. Li, H. Zhang, Y. Shen, S. M. Zakeeruddin, M. Graetzel, Y.-B. Cheng and M. Wang, *ACS Nano*, 2015, **9**, 1782–1787.
41 F. Zhou, Z. Ren, Y. Zhao, X. Shen, A. Wang, Y. Y. Li, C. Surya and Y. Chai, *ACS Nano*, 2016, **10**, 5900–5908.
42 J. Xu, Z. Ku, Y. Zhang, D. Chao and H. J. Fan, *Adv. Mater. Technol.*, 2016, **1**, 1600074–1600078.
43 F. Andre, F. Langer, J. Schwenzel and R. Kun, *Procedia Technol.*, 2014, **15**, 248–257.
44 M. Yu, W. D. McCulloch, Z. Huang, B. B. Trang, J. Lu, K. Amine and Y. Wu, *J. Mater. Chem. A*, 2016, **4**, 2766–2782.
45 Y. Song, X. Cheng, H. Chen, J. Huang, X. Chen, M. Han, Z. Su, B. Meng, Z. Song and H. Zhang, *J. Mater. Chem. A*, 2016, **4**, 14298–14306.
46 R. Elbersen, W. Vijselaar, R. M. Tiggelaar, H. Gardeniers and J. Huskens, *Adv. Mater.*, 2015, **27**, 6781–6796.
47 W. Zeng, X.-M. Tao, S. Chen, S. Shang, H. L. W. Chan and S. H. Choy, *Energy Environ. Sci.*, 2013, **6**, 2631–2638.
48 J.-H. Lee, K. Y. Lee, M. K. Gupta, T. Y. Kim, D.-Y. Lee, J. Oh, C. Ryu, W. J. Yoo, C.-Y. Kang, S.-J. Yoon, J.-B. Yoo and S.-W. Kim, *Adv. Mater.*, 2014, **26**, 765–769.
49 Z. He, B. Xiao, F. Liu, H. Wu, Y. Yang, S. Xiao, C. Wang, T. P. Russell and Y. Cao, *Nat. Photonics*, 2015, **9**, 174–179.
50 J.-D. Chen, C. Cui, Y.-Q. Li, L. Zhou, Q.-D. Ou, C. Li, Y. Li and J.-X. Tang, *Adv. Mater.*, 2015, **27**, 1132.
51 M. Ye, X. Wen, M. Wang, J. Iocozzia, N. Zhang, C. Lin and Z. Lin, *Mater. Today*, 2015, **18**, 155–162.
52 W. Chen, Y. Wu, Y. Yue, J. Liu, W. Zhang, X. Yang, H. Chen, E. Bi, I. Ashraful, M. Gratzel and L. Han, *Science*, 2015, **350**, 944–948.
53 P. Huang, J. Du, M. C. Biewer and M. C. Stefan, *J. Mater. Chem. A*, 2015, **3**, 6244–6257.
54 M. P. Bhatt, J. Du, E. A. Rainbolt, T. M. S. K. Pathiranage, P. Huang, J. F. Reuther, B. M. Novak, M. C. Biewer and M. C. Stefan, *J. Mater. Chem. A*, 2014, **2**, 16148–16156.
55 A. Fakharuddin, R. Jose, T. M. Brown, F. Fabregat-Santiago and J. Bisquert, *Energy Environ. Sci.*, 2014, **7**, 3952–3981.
56 P. Qin, P. Sanghyun, M. I. Dar, K. Rakstys, H. ElBatal, S. A. Al-Muhtaseb, C. Ludwig and M. K. Nazeeruddin, *Adv. Funct. Mater.*, 2016, **26**, 5550–5559.
57 T. Liu, J. Hou, B. Wang, F. Bai, H. Chen, L. Gao, Y. Cao, H. He, J. Wang, N. Wang, G. Cao and Z. Guo, *J. Mater. Chem. A*, 2016, **4**, 10794–10800.
58 H. He, C. Zhang, T. Liu, Y. Cao, N. Wang and Z. Guo, *J. Mater. Chem. A*, 2016, **4**, 9362–9369.
59 X. Liu, Y. Cheng, L. Wang, L. Cai and B. Liu, *Phys. Chem. Chem. Phys.*, 2012, **14**, 7098–7103.
60 S. Shi, J. Yuan, G. Ding, M. Ford, K. Lu, G. Shi, J. Sun, X. Ling, Y. Li and W. Ma, *Adv. Funct. Mater.*, 2016, **26**, 5669–5678.
61 J. Zhao, Y. Li, A. Hunt, J. Zhang, H. Yao, Z. Li, J. Zhang, F. Huang, H. Ade and H. Yan, *Adv. Mater.*, 2016, **28**, 1868–1873.
62 B. O'Regan and M. Grätzel, *Nature*, 1991, **353**, 737–740.
63 N. Yao, J. Huang, K. Fu, X. Deng, M. Ding, M. Shao and X. Xu, *Electrochim. Acta*, 2015, **154**, 273–277.
64 X. Liu, L. Wang, Z. Xue and B. Liu, *RSC Adv.*, 2012, **2**, 6393–6396.
65 H. Yu, S. Zhang, H. Zhao, G. Will and P. Liu, *Electrochim. Acta*, 2009, **54**, 1319–1324.
66 J. D. Roy-Mayhew and I. A. Aksay, *Chem. Rev.*, 2014, **114**, 6323–6348.
67 S. Zhang, X. Yang, Y. Numata and L. Han, *Energy Environ. Sci.*, 2013, **6**, 1443–1464.
68 J. Gong, J. Liang and K. Sumathy, *Renewable Sustainable Energy Rev.*, 2012, **16**, 5848–5860.
69 X. Yin, X. Liu, L. Wang and B. Liu, *Electrochem. Commun.*, 2010, **12**, 1241–1244.
70 D. Sengupta, P. Das, B. Mondal and K. Mukherjee, *Renewable Sustainable Energy Rev.*, 2016, **60**, 356–376.
71 Y. Hua, J. Zhang, B. Xu, P. Liu, M. Cheng, L. Kloo, E. M. J. Johansson, K. Sveinbjörnsson, K. Aitola, G. Boschloo and L. Sun, *Nano Energy*, 2016, **26**, 108–113.
72 J. Zhang, N. Vlachopoulos, M. Jouini, M. B. Johansson, X. Zhang, M. K. Nazeeruddin, G. Boschloo, E. M. J. Johansson and A. Hagfeldt, *Nano Energy*, 2016, **19**, 455–470.
73 I. Chung, B. Lee, J. He, R. P. H. Chang and M. G. Kanatzidis, *Nature*, 2012, **485**, 486–489.
74 A. T. Murray, J. M. Frost, C. H. Hendon, C. D. Molloy, D. R. Carbery and A. Walsh, *Chem. Commun.*, 2015, **51**, 8935–8938.
75 B. Xu, E. Gabrielsson, M. Safdari, M. Cheng, Y. Hua, H. Tian, J. M. Gardner, L. Kloo and L. Sun, *Adv. Energy Mater.*, 2015, **5**, 1402340–1402345.
76 Z. Huo, L. Tao, S. Wang, J. Wei, J. Zhu, W. Dong, F. Liu, S. Chen, B. Zhang and S. Dai, *J. Power Sources*, 2015, **284**, 582–587.
77 L. Tao, Z. Huo, Y. Ding, Y. Li, S. Dai, L. Wang, J. Zhu, X. Pan, B. Zhang, J. Yao, M. K. Nazeeruddin and M. Grätzel, *J. Mater. Chem. A*, 2015, **3**, 2344–2352.
78 A. Apostolopoulou, V. Nagygyörgy, J. Madarász, E. Stathatos and G. Pokol, *J. Therm. Anal. Calorim.*, 2015, **121**, 371–380.
79 P. Yang, X. Xiao, Y. Li, Y. Ding, P. Qiang, X. Tan, W. Mai, Z. Lin, W. Wu, T. Li, H. Jin, P. Liu, J. Zhou, C. P. Wong and Z. L. Wang, *ACS Nano*, 2013, **7**, 2617–2626.
80 Z. Yang, J. Deng, X. Sun, H. Li and H. Peng, *Adv. Mater.*, 2014, **26**, 2643–2647.
81 M. Peng and D. Zou, *J. Mater. Chem. A*, 2015, **3**, 20435–20458.
82 S. Pan, Z. Yang, P. Chen, J. Deng, H. Li and H. Peng, *Angew. Chem., Int. Ed.*, 2014, **53**, 6110–6114.
83 L. Qiu, S. He, J. Yang, F. Jin, J. Deng, H. Sun, X. Cheng, G. Guan, X. Sun, H. Zhao and H. Peng, *J. Mater. Chem. A*, 2016, **4**, 10105–10109.
84 D. Yu, Q. Qian, L. Wei, W. Jiang, K. Goh, J. Wei, J. Zhang and Y. Chen, *Chem. Soc. Rev.*, 2015, **44**, 647–662.
85 X. Wang, K. Jiang and G. Shen, *Mater. Today*, 2015, **18**, 265–272.

86 Y. Zhang, Y. Wang, L. Wang, C.-M. Lo, Y. Zhao, Y. Jiao, G. Zheng and H. Peng, *J. Mater. Chem. A*, 2016, **4**, 9002–9008.
87 H. Sun, Y. Jiang, S. Xie, Y. Zhang, J. Ren, A. Ali, S.-G. Doo, I. H. Son, X. Huang and H. Peng, *J. Mater. Chem. A*, 2016, **4**, 7601–7605.
88 Z. Yang, J. Deng, H. Sun, J. Ren, S. Pan and H. Peng, *Adv. Mater.*, 2014, **26**, 7038–7042.
89 C.-Y. Hsu, H.-W. Chen, K.-M. Lee, C.-W. Hu and K.-C. Ho, *J. Power Sources*, 2010, **195**, 6232–6238.
90 H.-W. Chen, C.-Y. Hsu, J.-G. Chen, K.-M. Lee, C.-C. Wang, K.-C. Huang and K.-C. Ho, *J. Power Sources*, 2010, **195**, 6225–6231.
91 H. Wei, Y. Wang, J. Guo, X. Yan, R. O'Connor, X. Zhang, N. Z. Shen, B. L. Weeks, X. Huang, S. Wei and Z. Guo, *ChemElectroChem*, 2015, **2**, 119–126.
92 H. Wei, C. He, J. Liu, H. Gu, Y. Wang, X. Yan, J. Guo, D. Ding, N. Z. Shen, X. Wang, S. Wei and Z. Guo, *Polymer*, 2015, **67**, 192–199.
93 T. N. Murakami, N. Kawashima and T. Miyasaka, *Chem. Commun.*, 2005, 3346–3348.
94 M. Skunik, P. J. Kulesza, N. Vlachopoulos, L. Häggman and A. Hagfeldt, *ECS Trans.*, 2011, **35**, 93–102.
95 H. Nagai and H. Segawa, *Chem. Commun.*, 2004, 974–975.
96 M. A. Mahmoudzadeh, A. R. Usgaocar, J. Giorgio, D. L. Officer, G. G. Wallace and J. D. W. Madden, *J. Mater. Chem. A*, 2016, **4**, 3446–3452.
97 T. Miyasaka and T. N. Murakami, *Appl. Phys. Lett.*, 2004, **85**, 3932–3934.
98 M. Skunik-Nuckowska, K. Grzejszczyk, P. J. Kulesza, L. Yang, N. Vlachopoulos, L. Häggman, E. Johansson and A. Hagfeldt, *J. Power Sources*, 2013, **234**, 91–99.
99 R. Narayanan, P. N. Kumar, M. Deepa and A. K. Srivastava, *Electrochim. Acta*, 2015, **178**, 113–126.
100 A. P. Cohn, W. R. Erwin, K. Share, L. Oakes, A. S. Westover, R. E. Carter, R. Bardhan and C. L. Pint, *Nano Lett.*, 2015, **15**, 2727–2731.
101 N. Bagheri, A. Aghaei, M. Y. Ghotbi, E. Marzbanrad, N. Vlachopoulos, L. Häggman, M. Wang, G. Boschloo, A. Hagfeldt, M. Skunik-Nuckowska and P. J. Kulesza, *Electrochim. Acta*, 2014, **143**, 390–397.
102 W. Guo, X. Xue, S. Wang, C. Lin and Z. L. Wang, *Nano Lett.*, 2012, **12**, 2520–2523.
103 J. Xu, H. Wu, L. Lu, S.-F. Leung, D. Chen, X. Chen, Z. Fan, G. Shen and D. Li, *Adv. Funct. Mater.*, 2014, **24**, 1840–1846.
104 C. Shi, H. Dong, R. Zhu, H. Li, Y. Sun, D. Xu, Q. Zhao and D. Yu, *Nano Energy*, 2015, **13**, 670–678.
105 H. Li, Q. Zhao, W. Wang, H. Dong, D. Xu, G. Zou, H. Duan and D. Yu, *Nano Lett.*, 2013, **13**, 1271–1277.
106 T. Chen, L. Qiu, Z. Yang, Z. Cai, J. Ren, H. Li, H. Lin, X. Sun and H. Peng, *Angew. Chem., Int. Ed.*, 2012, **51**, 11977–11980.
107 Y. Fu, H. Wu, S. Ye, X. Cai, X. Yu, S. Hou, H. Kafafy and D. Zou, *Energy Environ. Sci.*, 2013, **6**, 805–812.
108 R. Søndergaard, M. Hösel, D. Angmo, T. T. Larsen-Olsen and F. C. Krebs, *Mater. Today*, 2012, **15**, 36–49.
109 T. Kim, J.-H. Kim, T. E. Kang, C. Lee, H. Kang, M. Shin, C. Wang, B. Ma, U. Jeong, T.-S. Kim and B. J. Kim, *Nat. Commun.*, 2015, **6**, 8547.
110 H. Zhou, L. Yang and W. You, *Macromolecules*, 2012, **45**, 607–632.
111 L. Lu, T. Zheng, Q. Wu, A. M. Schneider, D. Zhao and L. Yu, *Chem. Rev.*, 2015, **115**, 12666–12731.
112 J.-S. Wu, S.-W. Cheng, Y.-J. Cheng and C.-S. Hsu, *Chem. Soc. Rev.*, 2015, **44**, 1113–1154.
113 Y. Li, *Acc. Chem. Res.*, 2012, **45**, 723–733.
114 G. Li, R. Zhu and Y. Yang, *Nat. Photonics*, 2012, **6**, 153–161.
115 G. Wee, T. Salim, Y. M. Lam, S. G. Mhaisalkar and M. Srinivasan, *Energy Environ. Sci.*, 2011, **4**, 413–416.
116 Z. Zhang, X. Chen, P. Chen, G. Guan, L. Qiu, H. Lin, Z. Yang, W. Bai, Y. Luo and H. Peng, *Adv. Mater.*, 2014, **26**, 466–470.
117 Z. L. Wang, G. Zhu, Y. Yang, S. Wang and C. Pan, *Mater. Today*, 2012, **15**, 532–543.
118 X. Wang, *Nano Energy*, 2012, **1**, 13–24.
119 J. Briscoe and S. Dunn, *Nano Energy*, 2015, **14**, 15–29.
120 Z. L. Wang, *Science*, 2006, **312**, 242–246.
121 Z. L. Wang, *Adv. Funct. Mater.*, 2008, **18**, 3553–3567.
122 R. Yang, Y. Qin, L. Dai and Z. L. Wang, *Nat. Nanotechnol.*, 2009, **4**, 34–39.
123 R. Yang, Y. Qin, C. Li, G. Zhu and Z. L. Wang, *Nano Lett.*, 2009, **9**, 1201–1205.
124 S. Xu, Y. Qin, C. Xu, Y. Wei, R. Yang and Z. L. Wang, *Nat. Nanotechnol.*, 2010, **5**, 366–373.
125 X. Li, Y. Chen, A. Kumar, A. Mahmoud, J. A. Nychka and H.-J. Chung, *ACS Appl. Mater. Interfaces*, 2015, **7**, 20753–20760.
126 Y.-F. Lin, J. Song, Y. Ding, S.-Y. Lu and Z. L. Wang, *Adv. Mater.*, 2008, **20**, 3127–3130.
127 Y. S. Zhou, R. Hinchet, Y. Yang, G. Ardila, R. Songmuang, F. Zhang, Y. Zhang, W. Han, K. Pradel, L. Montès, M. Mouis and Z. L. Wang, *Adv. Mater.*, 2013, **25**, 883–888.
128 C. K. Jeong, I. Kim, K.-I. Park, M. H. Oh, H. Paik, G.-T. Hwang, K. No, Y. S. Nam and K. J. Lee, *ACS Nano*, 2013, **7**, 11016–11025.
129 K.-I. Park, J. H. Son, G.-T. Hwang, C. K. Jeong, J. Ryu, M. Koo, I. Choi, S. H. Lee, M. Byun, Z. L. Wang and K. J. Lee, *Adv. Mater.*, 2014, **26**, 2514–2520.
130 Z. Pi, J. Zhang, C. Wen, Z. Zhang and D. Wu, *Nano Energy*, 2014, **7**, 33–41.
131 S. Shen and S. Hu, *J. Mech. Phys. Solids*, 2010, **58**, 665–677.
132 X.-Q. Fang, J.-X. Liu and V. Gupta, *Nanoscale*, 2013, **5**, 1716–1726.
133 X. Xue, S. Wang, W. Guo, Y. Zhang and Z. L. Wang, *Nano Lett.*, 2012, **12**, 5048–5054.
134 X. Xue, P. Deng, B. He, Y. Nie, L. Xing, Y. Zhang and Z. L. Wang, *Adv. Energy Mater.*, 2014, **4**, 1301329–1301333.
135 Y. Zhang, Y. Zhang, X. Xue, C. Cui, B. He, Y. Nie, P. Deng and Z. Lin Wang, *Nanotechnology*, 2014, **25**, 105401–105407.
136 L. Xing, Y. Nie, X. Xue and Y. Zhang, *Nano Energy*, 2014, **10**, 44–52.
137 Y.-S. Kim, Y. Xie, X. Wen, S. Wang, S. J. Kim, H.-K. Song and Z. L. Wang, *Nano Energy*, 2015, **14**, 77–86.
138 X. Xue, P. Deng, S. Yuan, Y. Nie, B. He, L. Xing and Y. Zhang, *Energy Environ. Sci.*, 2013, **6**, 2615–2620.

139 A. Ramadoss, B. Saravanakumar, S. W. Lee, Y.-S. Kim, S. J. Kim and Z. L. Wang, *ACS Nano*, 2015, **9**, 4337–4345.
140 R. Song, H. Jin, X. Li, L. Fei, Y. Zhao, H. Huang, H. Lai-Wa Chan, Y. Wang and Y. Chai, *J. Mater. Chem. A*, 2015, **3**, 14963–14970.
141 F. Wang, C. Jiang, C. Tang, S. Bi, Q. Wang, D. Du and J. Song, *Nano Energy*, 2016, **21**, 209–216.
142 Z. L. Wang, *ACS Nano*, 2013, **7**, 9533–9557.
143 F.-R. Fan, Z.-Q. Tian and Z. Lin Wang, *Nano Energy*, 2012, **1**, 328–334.
144 G. Zhu, Z.-H. Lin, Q. Jing, P. Bai, C. Pan, Y. Yang, Y. Zhou and Z. L. Wang, *Nano Lett.*, 2013, **13**, 847–853.
145 S. Wang, L. Lin, Y. Xie, Q. Jing, S. Niu and Z. L. Wang, *Nano Lett.*, 2013, **13**, 2226–2233.
146 P. Bai, G. Zhu, Y. Liu, J. Chen, Q. Jing, W. Yang, J. Ma, G. Zhang and Z. L. Wang, *ACS Nano*, 2013, **7**, 6361–6366.
147 G. Zhu, C. Pan, W. Guo, C.-Y. Chen, Y. Zhou, R. Yu and Z. L. Wang, *Nano Lett.*, 2012, **12**, 4960–4965.
148 S. Niu, Y. Liu, S. Wang, L. Lin, Y. S. Zhou, Y. Hu and Z. L. Wang, *Adv. Mater.*, 2013, **25**, 6184–6193.
149 G. Zhu, J. Chen, Y. Liu, P. Bai, Y. S. Zhou, Q. Jing, C. Pan and Z. L. Wang, *Nano Lett.*, 2013, **13**, 2282–2289.
150 N. Cui, L. Gu, Y. Lei, J. Liu, Y. Qin, X. Ma, Y. Hao and Z. L. Wang, *ACS Nano*, 2016, **10**, 6131–6138.
151 C. K. Jeong, K. M. Baek, S. Niu, T. W. Nam, Y. H. Hur, D. Y. Park, G.-T. Hwang, M. Byun, Z. L. Wang, Y. S. Jung and K. J. Lee, *Nano Lett.*, 2014, **14**, 7031–7038.
152 F.-R. Fan, L. Lin, G. Zhu, W. Wu, R. Zhang and Z. L. Wang, *Nano Lett.*, 2012, **12**, 3109–3114.
153 S. Wang, L. Lin and Z. L. Wang, *Nano Lett.*, 2012, **12**, 6339–6346.
154 H. Zhang, Y. Yang, Y. Su, J. Chen, K. Adams, S. Lee, C. Hu and Z. L. Wang, *Adv. Funct. Mater.*, 2014, **24**, 1401–1407.
155 H. Zhang, Y. Yang, T.-C. Hou, Y. Su, C. Hu and Z. L. Wang, *Nano Energy*, 2013, **2**, 1019–1024.
156 S. Zhai, H. E. Karahan, L. Wei, Q. Qian, A. T. Harris, A. I. Minett, S. Ramakrishna, A. K. Ng and Y. Chen, *Energy Storage Mater.*, 2016, **3**, 123–139.
157 L. Shi, X. Li, Y. Jia, D. Kong, H. He, M. Wagner, K. Müllen and L. Zhi, *Energy Storage Mater.*, 2016, **5**, 43–49.
158 A. G. Zestos, C. Yang, C. B. Jacobs, D. Hensley and B. J. Venton, *Analyst*, 2015, **140**, 7283–7292.
159 P. Xu, B. Wei, Z. Cao, J. Zheng, K. Gong, F. Li, J. Yu, Q. Li, W. Lu, J.-H. Byun, B.-S. Kim, Y. Yan and T.-W. Chou, *ACS Nano*, 2015, **9**, 6088–6096.
160 X. Pu, L. Li, M. Liu, C. Jiang, C. Du, Z. Zhao, W. Hu and Z. L. Wang, *Adv. Mater.*, 2016, **28**, 98–105.
161 X. Pu, L. Li, H. Song, C. Du, Z. Zhao, C. Jiang, G. Cao, W. Hu and Z. L. Wang, *Adv. Mater.*, 2015, **27**, 2472–2478.
162 S. Niu and Z. L. Wang, *Nano Energy*, 2015, **14**, 161–192.
163 X. Pu, M. Liu, L. Li, C. Zhang, Y. Pang, C. Jiang, L. Shao, W. Hu and Z. L. Wang, *Adv. Sci.*, 2016, **3**, 1500255–1500261.
164 Y. Yang, W. Guo, K. C. Pradel, G. Zhu, Y. Zhou, Y. Zhang, Y. Hu, L. Lin and Z. L. Wang, *Nano Lett.*, 2012, **12**, 2833–2838.
165 Y. Yang, Y. Zhou, J. M. Wu and Z. L. Wang, *ACS Nano*, 2012, **6**, 8456–8461.
166 C. R. Bowen, J. Taylor, E. LeBoulbar, D. Zabek, A. Chauhan and R. Vaish, *Energy Environ. Sci.*, 2014, **7**, 3836–3856.
167 Y. Yang, Z.-H. Lin, T. Hou, F. Zhang and Z. L. Wang, *Nano Res.*, 2012, **5**, 888–895.
168 Y. Yang, K. C. Pradel, Q. Jing, J. M. Wu, F. Zhang, Y. Zhou, Y. Zhang and Z. L. Wang, *ACS Nano*, 2012, **6**, 6984–6989.
169 S. R. Hunter, N. V. Lavrik, S. Mostafa, S. Rajic and P. G. Datskos, *Proc. SPIE*, 2012, 83770D–83770D14.
170 Y. Yang and Z. L. Wang, *Nano Energy*, 2015, **14**, 245–256.
171 Z. Wen, M.-H. Yeh, H. Guo, J. Wang, Y. Zi, W. Xu, J. Deng, L. Zhu, X. Wang, C. Hu, L. Zhu, X. Sun and Z. L. Wang, *Sci. Adv.*, 2016, **2**, e1600097.
172 C. Xu, X. Wang and Z. L. Wang, *J. Am. Chem. Soc.*, 2009, **131**, 5866–5872.
173 C. Xu and Z. L. Wang, *Adv. Mater.*, 2011, **23**, 873–877.
174 C. Pan, W. Guo, L. Dong, G. Zhu and Z. L. Wang, *Adv. Mater.*, 2012, **24**, 3356–3361.
175 S. Wang, X. Wang, Z. L. Wang and Y. Yang, *ACS Nano*, 2016, **10**, 5696–5700.
176 Y. Yang, H. Zhang, S. Lee, D. Kim, W. Hwang and Z. L. Wang, *Nano Lett.*, 2013, **13**, 803–808.
177 X. Li, Z.-H. Lin, G. Cheng, X. Wen, Y. Liu, S. Niu and Z. L. Wang, *ACS Nano*, 2014, **8**, 10674–10681.
178 Y. Zi, L. Lin, J. Wang, S. Wang, J. Chen, X. Fan, P.-K. Yang, F. Yi and Z. L. Wang, *Adv. Mater.*, 2015, **27**, 2340–2347.
179 Y. Yang, H. Zhang, G. Zhu, S. Lee, Z.-H. Lin and Z. L. Wang, *ACS Nano*, 2013, **7**, 785–790.
180 S. Wang, Z. L. Wang and Y. Yang, *Adv. Mater.*, 2016, **28**, 2881–2887.
181 J. Bae, Y. J. Park, M. Lee, S. N. Cha, Y. J. Choi, C. S. Lee, J. M. Kim and Z. L. Wang, *Adv. Mater.*, 2011, **23**, 3446–3449.
182 J.-H. Lee, J. Kim, T. Y. Kim, M. S. Al Hossain, S.-W. Kim and J. H. Kim, *J. Mater. Chem. A*, 2016, **4**, 7983–7999.

